



저작자표시-비영리-변경금지 2.0 대한민국

이용자는 아래의 조건을 따르는 경우에 한하여 자유롭게

- 이 저작물을 복제, 배포, 전송, 전시, 공연 및 방송할 수 있습니다.

다음과 같은 조건을 따라야 합니다:



저작자표시. 귀하는 원저작자를 표시하여야 합니다.



비영리. 귀하는 이 저작물을 영리 목적으로 이용할 수 없습니다.



변경금지. 귀하는 이 저작물을 개작, 변형 또는 가공할 수 없습니다.

- 귀하는, 이 저작물의 재이용이나 배포의 경우, 이 저작물에 적용된 이용허락조건을 명확하게 나타내어야 합니다.
- 저작권자로부터 별도의 허가를 받으면 이러한 조건들은 적용되지 않습니다.

저작권법에 따른 이용자의 권리는 위의 내용에 의하여 영향을 받지 않습니다.

이것은 [이용허락규약\(Legal Code\)](#)을 이해하기 쉽게 요약한 것입니다.

[Disclaimer](#)

공학석사 학위논문

**Morphological Manipulation of  
Cu<sub>2</sub>ZnSn(S,Se)<sub>4</sub> Thin Film Solar Cells  
Prepared by Galvanostatic  
Co-electrodeposition**

정전류 동시전기증착법으로 제작한 Cu<sub>2</sub>ZnSn(S,Se)<sub>4</sub>  
태양전지의 형상 조절 기술

2019년 2월

서울대학교 대학원

재료공학부

천기범

**Abstract**

**Morphological Manipulation of  
 $\text{Cu}_2\text{ZnSn}(\text{S},\text{Se})_4$  Thin Film Solar Cells  
Prepared by Galvanostatic  
Co-electrodeposition**

Kibeom Cheon

Department of Materials Science & Engineering

The Graduate School

Seoul National University

In this work, we manipulated the nucleation behavior in co-electrodeposition process of CZTSSe solar cell and suppressed the abnormal growth, without any additional post-process. We've also identified that the abnormal dendritic growth of the film is originated from the sparse dendritic nucleation of relatively Sn-rich Cu-Sn alloy, and making dense nucleation of Sn-rich alloy produced more uniform and smooth film

morphology. Root-mean square roughness ( $R_{\text{rms}}$ ) of the as-deposited copper-zinc-tin alloy decreased from 0.121  $\mu\text{m}$  to 0.068  $\mu\text{m}$  and  $R_{\text{rms}}$  of the CZTSSe thin-film after the chalcogenization process has decreased from 0.197  $\mu\text{m}$  to 0.140  $\mu\text{m}$ . Roughness controlled cells showed improved  $V_{\text{OC}}$  and fill factor, and this is regarded as a result of suppressed interface recombination. Transient photovoltage decay (TPVD) and  $V_{\text{OC}}$  - temperature measurement suggested that the interface recombination has decreased. The best device efficiency was 8.63%. This method is expected to reduce interface recombination of electrodeposited CZTSSe solar cell through geometrical approach, and also to contribute to tandem cell application.

**Keywords:** CZTSSe, Co-electrodeposition, Nucleation, Roughness, Interface Recombination

**Student Number:** 2017-23429

# Table of Contents

<b>Chapter 1. Introduction.....</b>	<b>1</b>
1.1 Current Status of Solar Energy Production.....	1
1.2 Photovoltaics: Principles and Materials.....	3
1.3 Development of CZTSSe Solar Cell.....	9
<b>Chapter 2. Background and Reviews.....</b>	<b>10</b>
2.1 Principles of CZTSSe Solar Cell.....	10
2.1.1 Physical Properties.....	10
2.1.2 Device Structure.....	12
2.1.3 Processes.....	13
2.2 Recent Researches and Developments in CZTSSe Solar Cell.....	23
2.3. Electrochemical Deposition.....	23

<b>Chapter 3. Experimental Details.....</b>	<b>29</b>
3.1 Fabrication.....	29
3.1.1 Back Contact.....	29
3.1.2 Absorber.....	30
3.1.3 Buffer, Window and Front Contact.....	30
3.2 Characterization.....	31
<b>Chapter 4. Results &amp; Discussion.....</b>	<b>34</b>
4.1 Materials Characterization.....	34
4.2 Device Characterization.....	50
<b>Chapter 5. Conclusions.....</b>	<b>64</b>
<b>Bibliography.....</b>	<b>65</b>
<b>국문초록.....</b>	<b>75</b>

# List of Figures

<b>Figure 1.1.1</b>	Solar PV generation capacity (Worldwide) in GW [2].....2
<b>Figure 1.2.1</b>	Schemes that represents principles of solar cells. Short circuit condition (left). General working condition (right).....6
<b>Figure 1.2.2</b>	Schematic representation of direct light absorption and indirect light absorption.....7
<b>Figure 1.2.3</b>	Shockley-Queisser detailed-balance efficiency limit as a function of band gap (black line) and 75% and 50% of the limit. The record efficiencies of various materials are marked depending on the band gap of the light absorbing materials. [6].....8
<b>Figure 2.1.1</b>	Band alignment of of CZTS, CZTSe and related materials. The red dotted line shows n-type pinning energy of fermi level [25].....15
<b>Figure 2.1.2</b>	Defect levels for various intrinsic point defect in bulk CZTS (top) and CZTSSe (bottom). Red energy states represent the acceptor level, and the blue ones represent the donor level [32].....16
<b>Figure 2.1.3</b>	<b>(a)</b> Effective mass of CZTS and CZTSSe. Subtext c represents conduction band, i.e. electron effective mass, and subtext v

	represents valence band, i.e. hole effective mass. $v_1, v_2, v_3$ means the index number from topmost valence band as shown in <b>(b)</b> : CZTS, and <b>(c)</b> : CZTSe [26].....	17
<b>Figure 2.1.4</b>	Phase stable region in chemical potential space. At different chemical potential of Cu. <b>(a),(b)</b> : CZTS <b>(c),(d)</b> : CZTSe. [32].....	18
<b>Figure 2.1.5</b>	Pseudo-ternary phase diagram of <b>(a)</b> $\text{Cu}_2\text{S-SnS}_2\text{-ZnS}$ system [138] and <b>(b)</b> $\text{Cu}_2\text{Se-SnSe}_2\text{-ZnSe}$ system [139] at 670 K.....	19
<b>Figure 2.1.6</b>	CZTS(e) crystal structure. (a) kesterite (b) stannite (c) wurtzite [55].....	21
<b>Figure 2.1.7</b>	Schematic device structure of CZTSSe solar cell.....	22
<b>Figure 3.1.1</b>	Schemes of the fabrication process in this experiment.....	33
<b>Figure 4.1.1</b>	<b>(a) ~ (d)</b> SEM images of as-deposited CZT alloy films on the Mo substrate depending on the operation time of initial stage, $t_i$ . <b>(a)</b> $t_i = 0$ s. <b>(b)</b> $t_i = 10$ s. <b>(c)</b> $t_i = 20$ s. <b>(d)</b> $t_i = 30$ s. <b>(e) ~ (h)</b> SEM images of CZTSSe films on the Mo substrate depending on $t_i$ . <b>(e)</b> $t_i = 0$ s. <b>(f)</b> $t_i = 10$ s. <b>(g)</b> $t_i = 20$ s. <b>(h)</b> $t_i = 30$ s.....	38
<b>Figure 4.1.2.</b>	Fault at the film caused by hydrogen bubble. (at $t_i = 30$ s condition) <b>(a)</b> as-deposited CZT alloy film, <b>(b)</b> CZTSSe films after annealing.....	39
<b>Figure 4.1.3</b>	<b>(a)</b> Histogram of particle size distribution (in area) depending	

	operation the time of initial stage ( $t_i$ ) (estimated from SEM images). Note that y-axis is presented in common log scale. <b>(b)</b> Corresponding particles processed from imageJ.....40
<b>Figure 4.1.4</b>	<b>(a)</b> AFM 3D reconstructed image (20 $\mu\text{m}$ x 20 $\mu\text{m}$ ) and <b>(b)</b> Root-mean-square roughness ( $R_{\text{rms}}$ ) of the films depending on $t_i$ . As-deposited CZT alloy film CZTSSe film after annealing process. In both cases, roughness was decreased as $t_i$ was increase.....41
<b>Figure 4.1.5</b>	<b>(a)</b> Voltage profile of conventional galvanostatic electro-deposition ( $t_i = 0$ s). <b>(b)</b> SEM images at $t \approx 58$ s, and its corresponding EDS elemental mapping. <b>(c)</b> Schematic diagram describing the change in film morphology in sequence.....42
<b>Figure 4.1.6</b>	Nucleation of Cu-Sn alloy under current density of -1.35mA/cm <sup>2</sup> . <b>(a)</b> $t = 0.5$ s, <b>(b)</b> 1.0 s, <b>(c)</b> 1.45 s, <b>(d)</b> 2.9 s.....43
<b>Figure 4.1.7.</b>	SEM images at total same charge of 800 mC (78.4 mC/cm <sup>2</sup> ). <b>(a)</b> ~ <b>(c)</b> -1.35 mA/cm <sup>2</sup> for 57.97 s. <b>(d)</b> ~ <b>(f)</b> -3.92 mA/cm <sup>2</sup> for 20 s.....44
<b>Figure 4.1.8</b>	TEM observation of deposited film at $t = 57.97$ s ( $j = -1.35\text{mA}/\text{cm}^2$ ). The deposited alloy was partially polycrystalline. The stoichiometry of alloys can be inferred from the EDS measurements. Large nuclei is expected to be $\text{Cu}_6\text{Sn}_5$ , and compact layer is expected to be $\text{Cu}_3\text{Sn}$ .....45

<b>Figure 4.1.9</b>	XRD pattern of <b>(a)</b> as-deposited CZT alloy film and <b>(b)</b> annealed CZTSSe (coupled $\theta$ - $2\theta$ scan).....	47
<b>Figure 4.1.10</b>	MoS <sub>2</sub> thickness of annealed CZTSSe films (a) $t_i = 0$ s, (b) $t_i = 30$ s.....	48
<b>Figure 4.1.11</b>	GIXRD pattern of annealed CZTSSe films.....	49
<b>Figure 4.2.1</b>	<b>(a)~(c)</b> Device characteristics of cells close to the median value depending on $t_i$ . <b>((a)</b> J-V measurement <b>(b)</b> EQE spectra <b>(c)</b> Device parameters).....	54
<b>Figure 4.2.2</b>	Statistical box plots of diode parameters depending on $t_i = 0$ s. <b>((a)</b> Shunt conductance <b>(b)</b> Series resistance <b>(c)</b> Ideality factor <b>(d)</b> Dark saturation current.....	55
<b>Figure 4.2.3</b>	Band gap energy estimated from the measured EQE spectra...56	
<b>Figure 4.2.4</b>	Carrier lifetime measured from transient photovoltage decay (b) $V_{OC}$ measured at different temperature points and activation energy ( $E_a$ ) estimated from extrapolation.....	57
<b>Figure 4.2.5</b>	Schematic band diagram of CZTSSe solar cell.....	58
<b>Figure 4.2.6</b>	<b>(a)</b> Best performing cells at each condition. <b>(b) ~ (e)</b> TEM observation of the device. <b>(b)</b> HAADF image of cross-sectional view. <b>(c)</b> CZTSSe/CdS interface. <b>(d)</b> EDS Line profile of elements. <b>(e)</b> Electron diffraction pattern.....	59
<b>Figure 4.2.7</b>	SAED pattern of CZTSSe. Plane indices and their corresponding	

	<i>d</i> -spacing.....	60
<b>Figure 4.2.8</b>	(a) ~ (c) Bright field TEM images of the device. (b) HR image at bulk CZTSSe (c) polycrystalline CdS.....	61
<b>Figure 4.2.9</b>	EDS mapping of the crosssection. (a) Integrated image, signals of (b) Cu (c) Zn (d) Sn (f) Cd.....	62
<b>Figure 4.2.10</b>	Statistical box plots of cell performances and factors depending on $t_i = (0 \text{ s}, 10 \text{ s}, 20 \text{ s}, 30 \text{ s})$ . (a) ~ (d) Applied current density: $-3.92 \text{ mA cm}^{-2} / -1.45 \text{ mA cm}^{-2}$ (e) ~ (h) Applied current density: $-3.92 \text{ mA cm}^{-2} / -1.35 \text{ mA cm}^{-2}$ for each stage. (1 <sup>st</sup> /2 <sup>nd</sup> ).....	63

# List of Tables

<b>Table 2.1.1</b>	Secondary phases of CZTS in general cases [45].....	20
<b>Table 2.3.1</b>	Categorization of electrochemical deposition processes fabricating CZTSSe solar cell [129].....	28
<b>Table 4.1.1</b>	Atomic composition of the films from EDS analysis.....	46

# Chapter 1. Introduction

## 1.1 Current Status of Solar Energy Production

In recent years, a social consensus that the conventional electric power generating methods, such as thermal power and nuclear power, need to be replaced to sustainable methods has been formed. Among the many alternatives, solar energy conversion has the advantages of simple structure, low-maintenance, scaling flexibility, and plentiful amount of the available energy source (1,575 ~ 48,837 EJ\* of available energy a year, which is 3.9 – 124 times of worldwide primary energy consumption in 2000[1]).

Solar energy generation has gradually increased in recent years. According to BP, [2] solar energy generation capacity has reached about 400 GW in 2017 (Figure 1.1.1), and actual energy generation has increased 35.2% in 2017 (from 328.2 TWh in 2016 to 442.6 TWh in 2017). This is quite rapid increase compared to the increase in worldwide primary energy consumption (2.2% in 2017) which shows the high potential of solar energy in the future.

---

\* EJ = exajoules =  $10^{12}$  J

## Solar PV generation capacity

Gigawatts, cumulative installed capacity

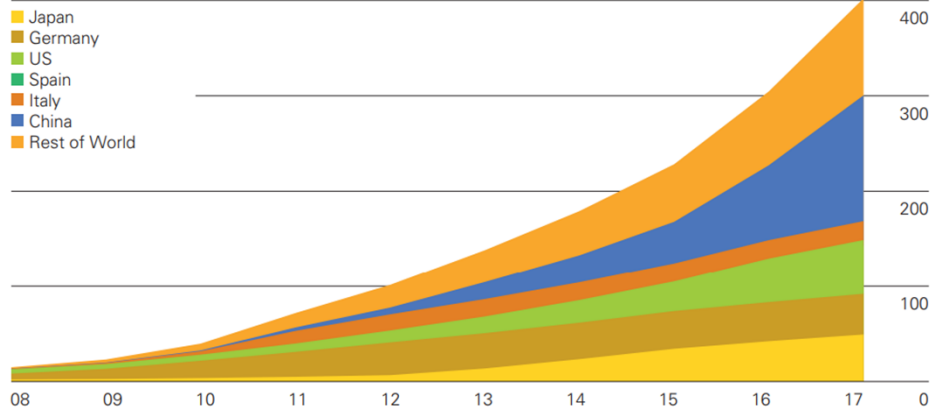


**Figure 1.1.1** Solar PV generation capacity (Worldwide) in GW. [2]

## 1.2 Photovoltaics: Principles and Materials

Solar cells, or photovoltaics, exploit the phenomena that electron is transitioned from a low energy state to a higher energy state when electromagnetic wave is applied on light absorbing semiconductor. This process is called carrier excitation or carrier generation. And the voltage generation effect from these excited carriers is called as “photovoltaic effect”.[3]

Usually, an excited electron at the conduction band is likely to be bound to the electrostatic attraction of a positive hole at the valence band. A bound electron-hole pair is called as an “exciton”. If the energy level is flat over the space, excitons will not be separated but will be collapsed because of their electrostatic attraction. However they can be separated when external electric field is applied and it is supplied from the built-in potential of the p-n junction.

In short, solar cells generate electrical energy through optical transition of electrons. But there are some factors limiting the efficiency, even at the ideal condition. If the electron is transitioned to much higher level to the band edge, it is likely to lose its energy through thermal relaxation. Also, low energy below bandgap cannot be absorbed. From these facts, William Shockley and Hans J. Queisser had calculated the theoretical efficiency limit from the solar spectrum approximated as 6000 K black body radiation, considering below-bandgap photons and relaxation of high energy carriers. This is called Shockley-Queisser (S-Q) limit or detailed balance limit,

a value about early 30% at 1.34 eV. [4, 5] S-Q limit depending on the band gap is presented on Figure 1.2.3. [6]

Many kinds of materials have been applied to photovoltaics so far, and those materials can be divided roughly into 3 generations.

First generation - crystalline silicon (c-Si) solar cells, and GaAs solar cells. Thanks to the splendid improvement in silicon transistor and integrated circuit technology, c-Si solar cell could've been easily developed from the early stage.[7] However, their indirect band gap nature which has a shortage of low absorptivity requires thickness over than 10  $\mu\text{m}$  scale to absorb sufficient lights. Although GaAs has an advantage of direct bandgap and high efficiency, difficulty in the process and expensive cost makes it difficult to be commercialized.

Second generation - amorphous silicon (a-Si) solar cells,  $\text{Cu(In,Ga)S}_2$  (CIGS) solar cells, and CdTe solar cells. a-Si solar cells made it possible to fabricate flexible solar cells. But their efficiency is far below than the c-Si. Although CIGS and CdTe solar cells have demonstrated high efficiency, they suffer from issues such as scarcity of In and toxicity of Cd.[8, 9]

Third generation - dye sensitized solar cells (DSSC), lead halide perovskite solar cells (PSC), organic solar cells (OSC), quantum dot solar cells (QDSC),  $\text{Cu}_2\text{ZnSn(S,Se)}_4$  solar cells, and so on. Those materials have been emerged to solve the problems that the conventional cells have. Among those, DSSC gathered much

interest as it was easy to fabricate and applicable to flexible or semitransparent devices. But it showed much lower efficiencies compared to the conventional ones, and also has critical issue in stability.[10] PSC, originated from DSSC, has been most popular materials of the third generation because of its many advantages. It has direct tunable bandgap, high absorption coefficient, and has shown rapid growth of efficiency in recent years. But it also has some problems such as instability and Pb toxicity.[11, 12] OSC also showed much possibilities in flexible and semitransparent applications using conducting polymer or molecules. However it has much difficulties in exciton separation since the excitons are much more strongly confined than ionic materials. It also has issues of stability.[13] QDSC has weird strengths of harvesting hot carrier energies through multiple exciton generation. But it also has issues in charge collection because of its complicated non-planar structure.[14]  $\text{Cu}_2\text{ZnSn}(\text{S},\text{Se})_4$  solar cells, which is derived from the CIGS solar cells, has advantages in non-toxic and earth-abundant nature. But it suffers from large open-circuit voltage ( $V_{OC}$ ) deficit which originated from tail state in bulk, interface recombination, and secondary phases.[15, 16]

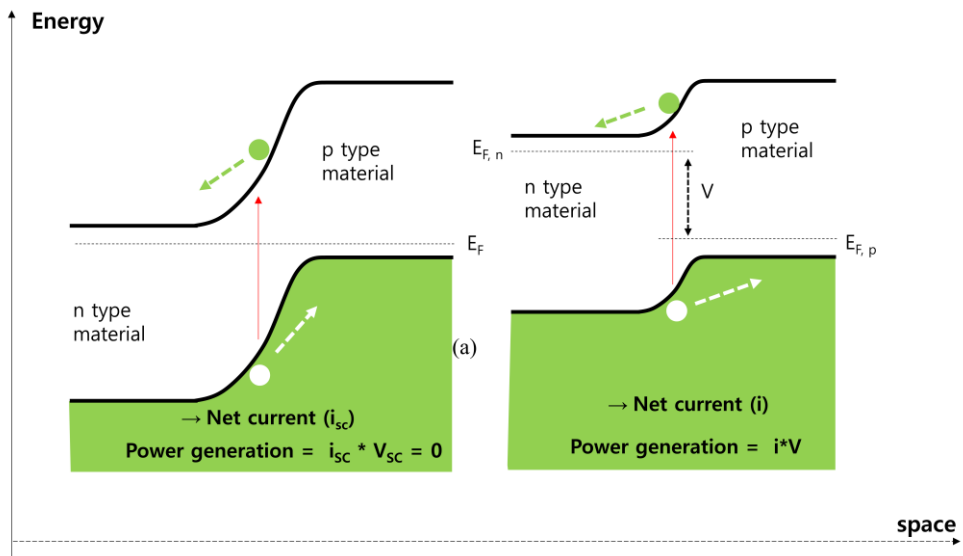


**Figure 1.2.1** Schemes that represents principles of solar cells. Short circuit condition (left). General working condition (right).

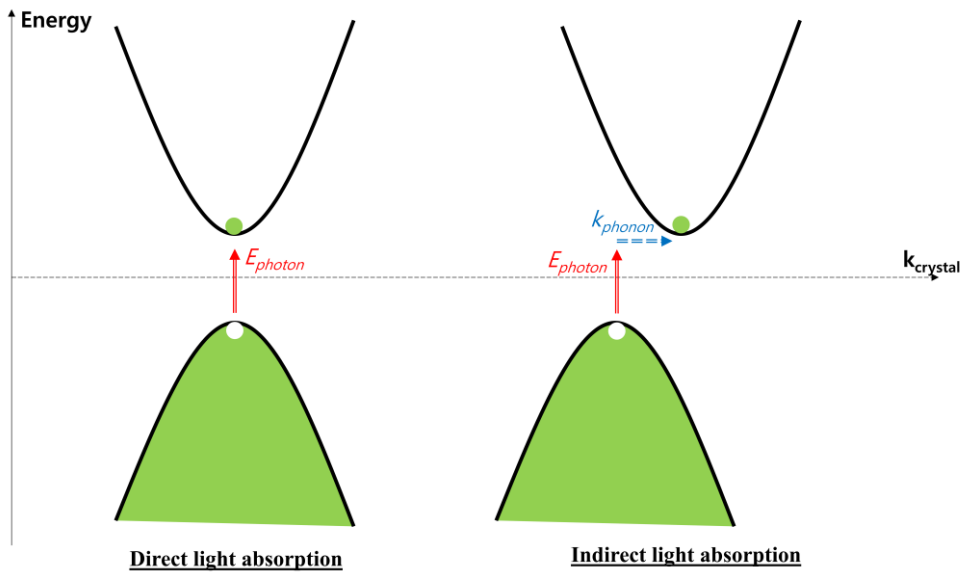


**Figure 1.2.2** Schematic representation of direct light absorption and indirect light absorption.

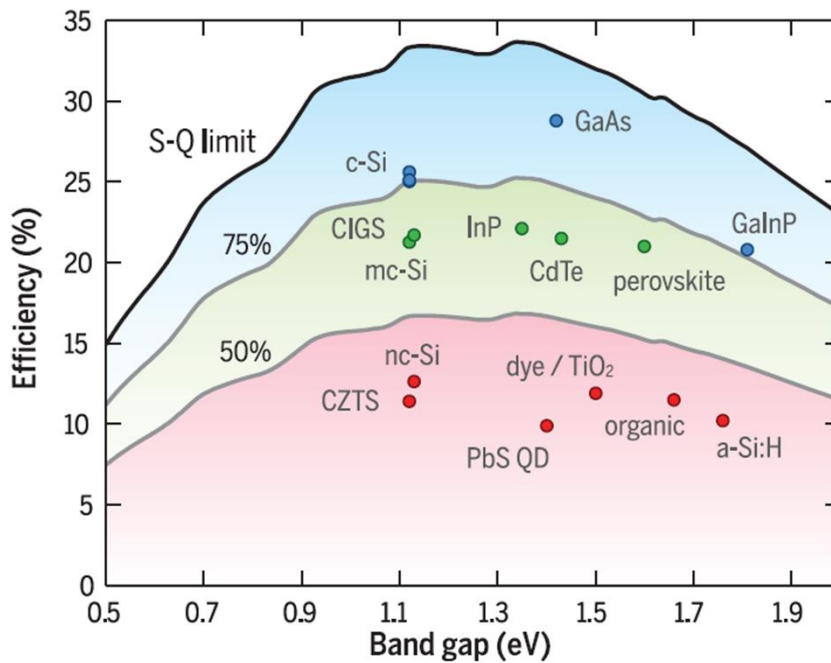


**Figure 1.2.3** Shockley-Queisser detailed-balance efficiency limit as a function of band gap (black line) and 75% and 50% of the limit. The record efficiencies of various materials are marked depending on the band gap of the light absorbing materials. [6]

### 1.3 Development of $\text{Cu}_2\text{ZnSn}(\text{S},\text{Se})_4$ (CZTSSe) Solar Cell

Although the conventional chalcogenide thin film solar cells such as CIGS and CdTe solar cells have been studied extensively and intensively, these types of solar cells have to solve some critical issues to be applied in real life -scarcity of In, Ga and toxicity of Cd.  $\text{Cu}_2\text{ZnSnS}_4$  (CZTS) or  $\text{Cu}_2\text{ZnSn}(\text{S},\text{Se})_4$  (CZTSSe) solar cell has emerged to solve those problems, which consists of earth-abundant and non-toxic elements.[15-17]

The photovoltaic effect of the CZTS was observed for the first time in 1988[18], and the first CZTS solar cell of 0.66% efficiency was fabricated by Katagiri et al[19]. They reported those CZTS as stannite ( $\bar{1}\bar{4}2m$ ) but it is considered as kesterite ( $\bar{1}\bar{4}$ ) these days since kesterite turned out to be thermodynamically the most stable phase. And this confusion is possible because of their symmetrical similarities. Since the first development of CZTS solar cell, the efficiency has increased fast in late 2000 ~ early 2010. Record breaking researches were done mainly by IBM group. [20-23]

## Chapter 2. Background and Reviews

### 2.1 Principles of CZTSSe Solar Cell

#### 2.1.1 Physical Properties

Kesterite CZTSSe is semiconducting material with a band gap of 1.0 eV for CZTSe, and 1.5 eV for CZTS (Figure 2.1.1) [24, 25]. Absorption coefficient ( $\alpha$ ) of the CZTS(e) is over  $10^4 \text{ cm}^{-1}$  scale from the computational approach [26], or many experimental researches.[27, 28] It has many kinds of point defect including vacancies and antisites. Types of point defects and its energy level in band gap is presented on Figure 2.1.2. Among them,  $V_{\text{Cu}}$  and  $\text{Cu}_{\text{Zn}}$  are the dominant shallow acceptor defects in CZTSe, which generate holes and giving p-type nature to the material. [29-33]

Potential fluctuation can also be found in CZTSSe. In general, disorder from the amorphous nature of the material, or heavy concentration of doped impurity / intrinsic point defect can cause potential fluctuation of the materials [34-36]. This potential fluctuation is reported for many materials including hydrogenated a-Si [37, 38], heavily doped GaAs [39], and also CIGS [40]. CZTSSe especially shows large magnitude of potential fluctuation caused from the high density intrinsic point defects and defect complexes such as  $[\text{Cu}_{\text{Zn}}^- + \text{Zn}_{\text{Cu}}^+]$  [41]. Potential fluctuation of CZTSSe makes tail-state in band gap, which causes band-gap narrowing effect.

Broad peak of Photoluminescence measurements and red-shift of the peak suggest the existence of band tailing. [41, 42] The potential fluctuation amplitude ( $\gamma_{opt}$ ) about 170 meV was obtained from the photo-luminescence measurement of CZTS. [43] Dielectric constant also contributes to the large fluctuation of the band. Their relationship is given as follows. [40]

$$\gamma_{opt}^5 = \left( \frac{e^2}{4\pi\epsilon_r\epsilon_0} \right)^4 \frac{N_t^2 \hbar^2}{m_r}$$

$\epsilon_r$ : dielectric constant,  $\epsilon_0$ : vacuum permittivity

$N_t$ : charged defect density,

$m_r$ : electron – hole reduced effective mass

As the experimental value for the dielectric constant of CZTSSe is smaller than that of CIGS, it may create much larger fluctuation of the band in addition to higher density of charged defects. [41]

Computational studies [26, 44] have reported the effective mass of CZTS near  $k=0$ . Effective mass of hole is about 0.2-0.7  $m_e$  for CZTS and 0.1-0.5  $m_e$  for CZTSe depending on the belonged band and direction. Effective mass of the electron is much lighter than the one of hole; 0.2  $m_e$  for CZTS and 0.1  $m_e$  for CZTSe. (Figure 2.1.3)

Because of the narrow region of stability (Figure 2.1.4, Figure 2.1.5), CZTSSe is also likely to be formed with lots of secondary phases such as  $Cu_2(S,Se)$ ,  $Zn(S,Se)$ ,  $Sn(S,Se)$  (Table 2.1.1). Especially,  $Cu_2(S,Se)$  is known as semi-metallic material, which are likely to make short circuit.  $Zn(S,Se)$  is known as n-type widegap

semiconductor which can increase series resistance [45]. To eliminate those secondary phases, KCN etching (for Cu-rich secondary phases) [46-49] and HCl etching (for Zn(S,Se)) [50] are generally used process as guaranteed techniques. And other chemicals such as  $(\text{NH}_4)_2\text{S}$  [51],  $\text{H}_2\text{O}_2$  [52], and even mechanical exfoliation method [53] are studied for selective removal of those secondary phases.

CZTSSe generally shows three types of crystal structures, kesterite ( $\bar{1}\bar{4}$ ), stannite ( $\bar{1}\bar{4}2m$ ) and wurtzite (Pc)[54-56], (Figure 2.1.6). It is known that the kesterite phase is most stable state and that CZTSSe crystallize into kesterite phase in general, but usually it is difficult to distinguish from the stannite because of symmetrical similarities and Cu-Zn disorder[57, 58]. Completely disordered kesterite has space group of  $\bar{1}\bar{4}2m$ , which is identical to the stannite.[42] Wurtzite (WZ) phase can also be divided into WZ-derived kesterite (WZ-KS) and WZ-derived stannite (WZ-ST). As WZ is metastable one compared to zinc-blend derived phases (kesterite or stannite), it is necessary to control the kinetics of crystal growth to get the WZ phase, which usually observed in nanocrystals or nanorods. [31, 56, 59]

### **2.1.2 Device Structure**

Device structure of CZTSSe solar cell is presented on Figure 2.1.7. Mo has been used as back contact of the conventional CIGS solar cell because of its suitable work function, mechanical strength and natural  $\text{MoS}_2$  formation making ohmic contact. But many researchers reported that in CZTSSe device  $\text{MoS}_2$  can be detrimental

because of it forms schottky barrier to absorber [60], and also can cause phase segregation to the secondary phases [61]. To overcome this drawbacks, lots of researches including implanting intermediate layer, such as TiN [62, 63], ZnO [64], carbon [65], or even transferring CZTSSe from Mo to MoO<sub>3</sub>/Au substrate [66, 67] have been done.

CdS is widely used as n-type buffer, which makes p-n junction with absorber, at many thin film photovoltaics including CIGS and CdTe solar cells. But its toxicity also has been an issue for commercialization. Non-toxic materials such as ZnO [68], ZnS [69, 70], Zn<sub>1-x</sub>Sn<sub>x</sub>O [71] and In<sub>2</sub>S<sub>3</sub> [72, 73] are studied as alternatives. [74, 75]. Also, recombination at CZTSSe/CdS heterojunction interface is regarded as a major cause of large V<sub>OC</sub> deficit in CZTSSe solar cell. [15, 60, 76, 77]

Intrinsic ZnO (i-ZnO) is generally used as an intermediate layer between CdS and TCO. Its electrically insulating nature helps to block shunt path and generally i-ZnO under 100 nm of thickness reported as not detrimental on the charge collection. [78, 79]. Atomic layer deposited Al<sub>2</sub>O<sub>3</sub> was also studied as an intermediate layer. [80]. Generally, Aluminum doped ZnO (AZO) and Ni/Al are used as TCO and front contact each.

### **2.1.3 Processes**

Lots of fabrication processes for CZTSSe have developed including evaporation [81-83], electron-beam evaporation [19], sputtering [84-86], pulsed laser deposition

[87], spray pyrolysis [88-90], electrodeposition [91, 92], and spin-coating based approach (aqueous/non-aqueous solution [93-95], nanocrystals/powder dispersion [96, 97], and hydrazine process [23]). Although the hydrazine based approach has achieved the record efficiency of 12.6%, it is considerably low efficiency compared to CIGS solar cell, and also it even didn't get to 50% of the S-Q limit.

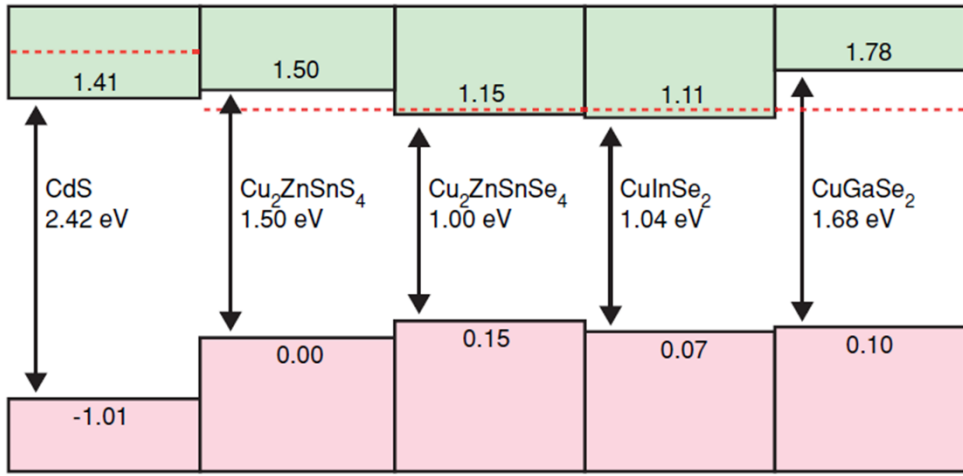


**Figure 2.1.1** Band alignment of of CZTS, CZTSe and related materials. The red dotted line shows n-type pinning energy of fermi level. [25]

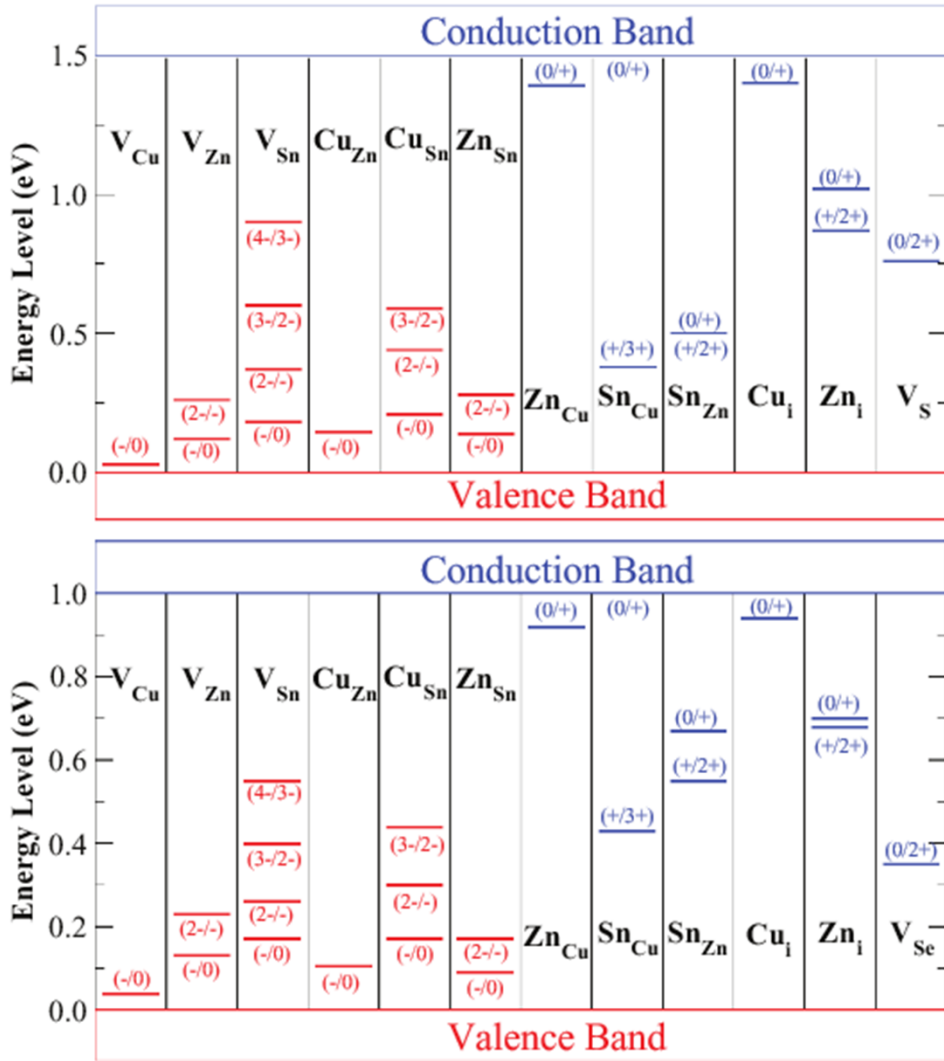


**Figure 2.1.2** Defect levels for various intrinsic point defect in bulk CZTS (top) and CZTSSe (bottom). Red energy states represent the acceptor level, and the blue ones represent the donor level. [32]

(a)

	$\text{Cu}_2\text{ZnSnS}_4$		$\text{Cu}_2\text{ZnSnSe}_4$	
	Kesterite	Stannite	Kesterite	Stannite
$m_{c1}^\perp [m_0]$	0.18	0.17	0.08	0.06
$m_{c1}^\parallel [m_0]$	0.20	0.18	0.08	0.06
$m_{v1}^\perp [m_0]$	0.71	0.33	0.33	0.09
$m_{v1}^\parallel [m_0]$	0.22	0.84	0.09	0.66
$m_{v2}^\perp [m_0]$	0.35	0.27	0.09	0.15
$m_{v2}^\parallel [m_0]$	0.52	0.88	0.50	0.09
$m_{v3}^\perp [m_0]$	0.26	0.73	0.24	0.29
$m_{v3}^\parallel [m_0]$	0.76	0.17	0.28	0.15

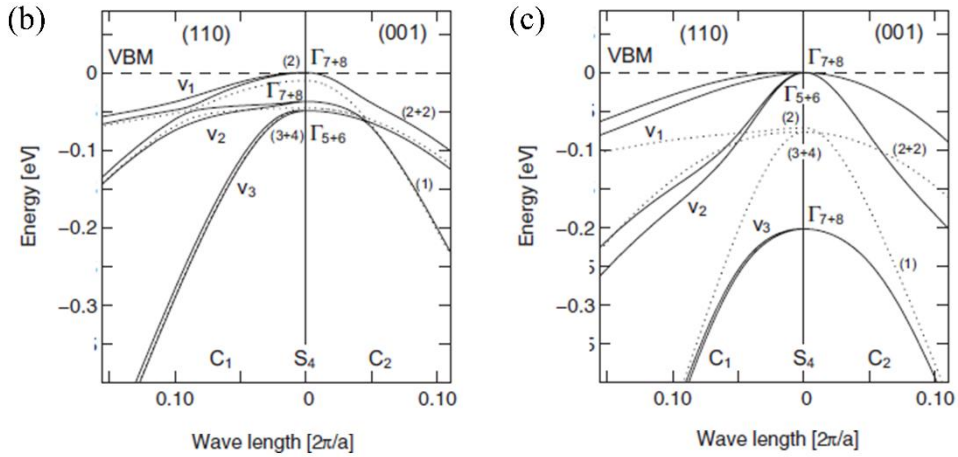


**Figure 2.1.3 (a)** Effective mass of CZTS and CZTSSe. Subtext c represents conduction band, i.e. electron effective mass, and subtext v represents valence band, i.e. hole effective mass. v1,v2,v3 means the index number from topmost valence band as shown in **(b)**: CZTS, and **(c)**: CZTSe. [26]

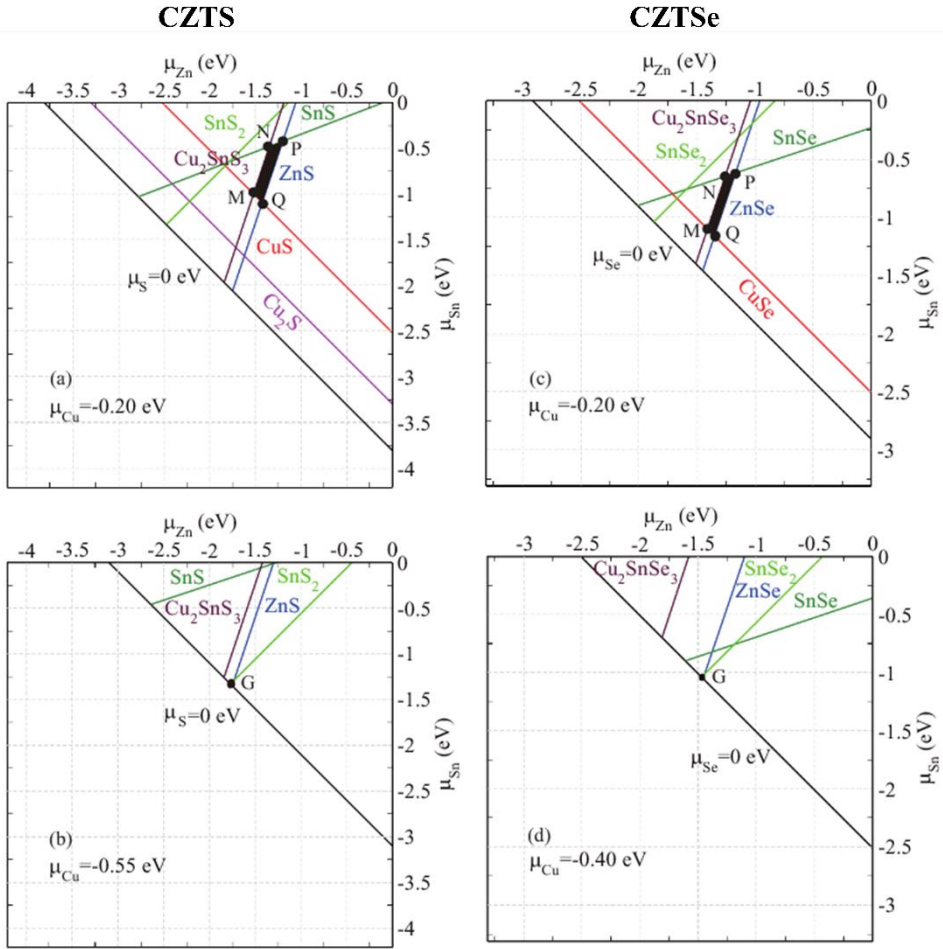


**Figure 2.1.4** Phase stable region in chemical potential space. At different chemical potential of Cu. (a),(b): CZTS (c),(d): CZTSe. [32]

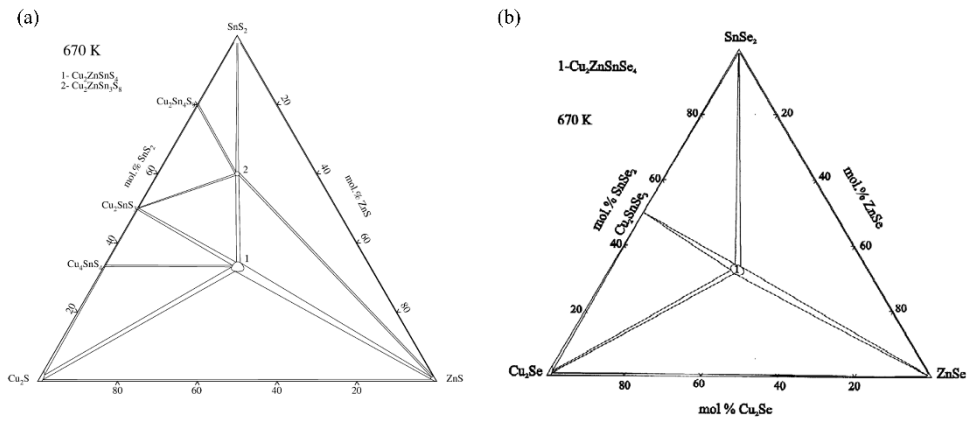


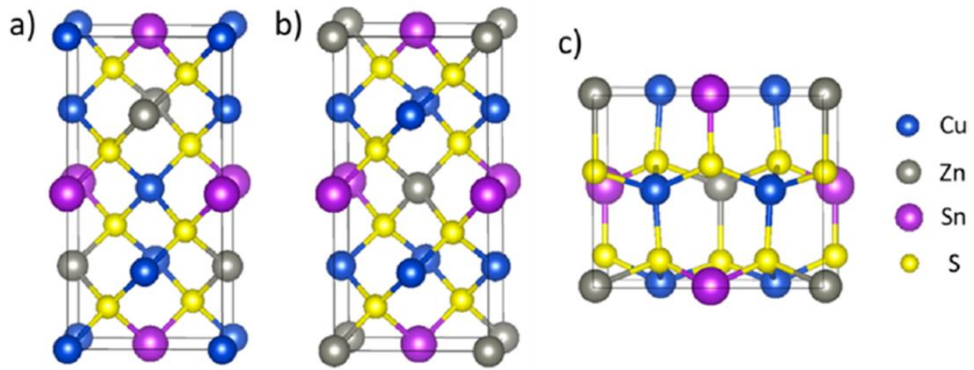
**Figure 2.1.5** Pseudo-ternary phase diagram of (a)  $\text{Cu}_2\text{S}-\text{SnS}_2-\text{ZnS}$  system [138] and (b)  $\text{Cu}_2\text{Se}-\text{SnSe}_2-\text{ZnSe}$  system [139] at 670 K.

Properties	$\text{Cu}_2\text{ZnSnS}_4$	ZnS
Band gap	$\sim 1.45$ eV	3.54–3.68 eV
Electrical properties	Semiconductor, p-type	Insulator
Structural properties	Kesterite	Sphalerite and wurtz
Impact on solar cell performance	Essential absorbing material	Insulating, reduces device active area

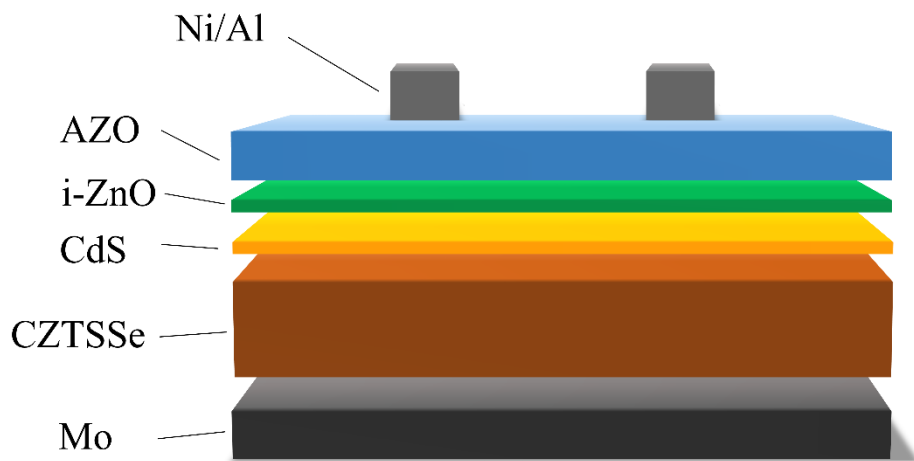
  

$\text{Cu}_2\text{S}$	$\text{SnS}_2$	$\text{Cu}_2\text{SnS}_3$
1.21 eV	2.2 eV	0.98–1.35 eV
p-Type, metal like, and highly defective Chalcocite	n-Type	p-Type
Metallic and short solar cell	Rhombohedral n-type, forms diodes and barriers for carrier collection	Cubic and tetragonal Affects carrier collection efficiency

**Table 2.1.1** Secondary phases of CZTS in general cases. [45]



**Figure 2.1.6** CZTS(e) crystal structure. (a) kesterite (b) stannite (c) wurtzite. [55]



**Figure 2.1.7** Schematic device structure of CZTSSe solar cell.

## 2.2 Recent Researches and Developments in CZTSSe Solar Cell

CZTSSe solar cells have suffered from large  $V_{OC}$  deficit. There are many factors that pull down the open circuit voltage of CZTSSe solar cells. Deep level point defect such as  $Sn_{Cu}$ ,  $Sn_{Zn}$ ,  $Zn_i$ , and  $V_S$  are known to work as recombination center [36, 98], and also Cu-Zn disorder known to have detrimental effect on device performance. To suppress these point defect, doping or substituting cations are attempted. Na[99, 100], Li [95, 101, 102], K [103], Sb [104], Ag[105, 106], Cd[107, 108], Ge[89, 109, 110] were studied as dopant or substitutional cations for CZTSSe. Some researchers have studied and tried perfect substitution, which making another novel quaternary I<sub>2</sub>-II-IV-VI<sub>4</sub> semiconductor design [111, 112] such as  $Ag_2ZnSn(S,Se)_4$  [113, 114],  $Cu_2CdSn(S,Se)_4$  [115],  $Cu_2BaSn(S,Se)_4$  [116-118], and  $Cu_2ZnGe(S,Se)_4$  [119, 120]. However none of them has achieved the efficiency of CZTSSe yet.

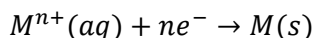
Interface recombination through CZTSSe/CdS heterojunction is considered as a major cause of large  $V_{OC}$  deficit.  $Al_2O_3$  [80, 121],  $TiO_2$  [122],  $SnO_2$  [123],  $Zn(S,O)$  [124] were introduced as an intermediate layer to passivate surface state of CZTSSe. Also, post-deposition annealing process was also applied to suppress the interface recombination [86, 125, 126].

## 2.3 Electrochemical Deposition

In order to commercialize CZTSSe solar cells, we need cheap and scalable

processes. Spray deposition [90], inkjet printing[127] , blade/knife coating[96] are regarded as scalable process for commercialization. And ‘electrochemical deposition’ or ‘electrodeposition’ is also considered as one of the most commercially promising processes because of its simplicity, scalability, cost-effectiveness, and high precursor usage.

Electrodeposition is film deposition process through reduction or oxidation reaction, occurred by applied potential from power supply or electrochemical apparatus such as potentiostat. For example, metal electrodeposition needs reductive current for electrodeposition. When negative potential is applied on the working electrode, cations are reduced at the electrode. This electrode is called as cathode, where the reduction reaction takes place. At counter electrode, oxidation half reaction occurs such as oxygen evolution. This electrode is called as anode, where the oxidation reaction takes place. In reaction equation,

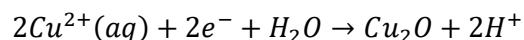


for working electrode. Thus, in metal electrodeposition, working electrode is cathode and counter electrode is anode.

Consider a case of oxide materials. In this case, cathodic or anodic electrodeposition can be used in complementarily. For example, MnO<sub>2</sub> deposition from Mn<sup>2+</sup> reaction is represented as [128]

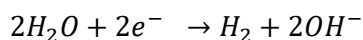


This is anodic electrodeposition since Mn is oxidized giving electrons to the electrode. In contrast, Cu<sub>2</sub>O deposition from Cu<sup>2+</sup> is represented as

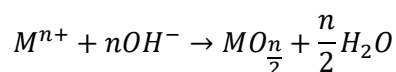
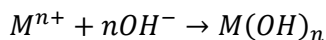


Suggesting cathodic electrodeposition. The key argument that determining what kind of electrodeposition is needed to deposit the target material is valence state difference. If partial oxidation is needed, we should adopt anodic electrodeposition. If partial reduction is needed, we should adopt cathodic electrodeposition. Therefore, for electrodeposition of oxides, the working electrode can be either cathode or anode depending on which strategy you take. [128]

We can also get oxide from manipulating local pH at working electrode. When cathodic potential is applied on working electrode, water (or nitrate ion if you've put in it) tends to be reduced generating OH<sup>-</sup>.



As several metal ions forms insoluble salts of hydroxide or oxide in high pH, metal hydroxide or oxide is deposited near the working electrode, depending on its chemical nature.



This process doesn't change the valence state of metal elements. However, the

working electrode is cathode, because the water is reduced as getting electrons from the electrode. [128]

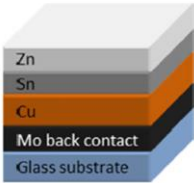
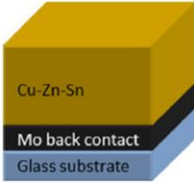
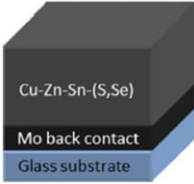
There are mainly three types of CZTSSe electrodeposition (Table 2.3.1) [129]. First, sequentially depositing three Cu, Sn, Zn components [91, 130, 131]. This is also called as stacked elemental layer (SEL) electrodeposition. This method shows advantages in easy control of Cu-Sn-Zn stoichiometry and also fabricating dense layers, but has shortages like non-uniform elemental composition in depth and onerous 3-step process.

Second, depositing Cu, Sn, Zn at the same time in one-pot (metal co-electrodeposition) [92, 132], then make the precursor films react to chalcogen in order for getting CZTSSe. This process is more convenient for fabricating CZTSSe than the previous one, but the process optimization is difficult since the standard reduction potential differences are very large. This makes fine stoichiometric manipulation difficult.

Third, depositing CZTSSe directly from the one-pot electrodeposition (Quaternary co-electrodeposition)[133, 134]. This is most convenient process design of those three, but has many technical difficulties such as large potential difference, bath stability issue, and it usually needs additional chalcogenization step since chalcogen elements are likely to be off-stoichiometry at as-electrodeposited condition.

Electrodeposition also has several weakness. Process optimizing (especially for co-

electrodeposition) known to be difficult, even in a case of CIGS fabrication.[8] For CZTSSe, it is more difficult since the standard reduction potential differences are much larger. Electrodeposited CZTSSe also shows abnormal dendritic growth and rough morphology [135, 136], which is detrimental on the device performance because it provides more interface recombination sites [129, 130]. Rough morphology is a problematic obstacle for a monolithic multi-junction application as roughness makes it tricky to form additional layers on them and can also cause cell failure because it is obvious that protrusions on the bottom cell are likely to work as a shunt path. [137]

process	strengths	weaknesses	opportunities	threats
Section 3.2 Stacked elemental layer (SEL) electrodeposition 	+ dense layers + easy control of stoichiometry + different stack orderings possible + short deposition times + stable electrolytes	– 3 steps – in-depth inhomogeneity (need for interdiffusion/mixing) – one preferred stack order (Cu/Sn/Zn)	+ more degrees of freedom (stoichiometry, stack ordering, density...) + process more easily adaptable for industry	– if the precursor is required to contain chalcogen for the highest quality semiconductor material this process may need co-deposition of metal chalcogen for at least one layer
Section 3.3 metal alloy co-electrodeposition 	+ single bath + minimum of equipment + short deposition times	– multiple diffusion coefficients and deposition potentials mean homogeneous deposition on $\text{cm}^2$ areas is difficult	+ control of as-deposited Cu-Sn and Cu-Zn alloys and alloy particle size	– electrolyte bath chemistry difficult to control to give uniform compositions over large areas
Section 3.4 chalcogenide co-electrodeposition 	+ single bath + minimum of equipment	– as for alloy deposition and additionally: – no stable or replenishable chalcogen source – long deposition times	+ if a precursor containing sulfur or selenium shows superior semiconductor properties after annealing	– too many technical difficulties to surmount to provide uniform material even on areas of $\text{cm}^2$

**Table 2.3.1** Categorization of electrochemical deposition processes fabricating CZTSSe solar cell. [129]

## Chapter 3. Experimental Details

As mentioned in the previous chapter, large roughness of absorber can be detrimental to carrier lifetime and also a hurdle for tandem application. In order to overcome those, we strategically separated nucleation stage and growth stage. As initially applying high current density, we manipulated the nucleation behavior and could suppress the abnormal growth. The details of experimental procedure is described in this chapter. (Figure 3.1.1)

### 3.1 Fabrication

#### 3.1.1 Back Contact

Soda lime glass substrate (100 mm x 100 mm x 1.1 mm) was sonicated by acetone and ethanol successively, then dried with N<sub>2</sub> blowing. The glass was UV-ozone treated for 10 min to eliminate residual organic contaminant. Mo back contact layer was sputtered on the substrate. Its deposited thickness was about 600 nm.

Mo-coated glass was divided into 6 pieces. It was cleaned with diluted detergent (5v/v% of Hellmanex, Sigma-Aldrich) and deionized (DI) water. Then it was taped to confirm the electrodeposition area as 3 cm x 3.4 cm. Edge of the substrate was painted with commercial manicure to prevent overconcentration of electric field at the edge.

### 3.1.2 Absorber

Co-electrodeposition of CZT alloy films were performed on the Mo-coated soda lime glass using conventional three electrode system in galvanostatic mode (Counter electrode: 4 cm × 6 cm Pt plate, Reference electrode: Ag/AgCl [3 M NaCl], Potentiostat: PARSTAT MC, Princeton applied research, the temperature was kept as 20 °C using jacketed beaker.

The deposition was done sequentially in two stages, initial stage of high current density (-3.92 mA cm<sup>-2</sup>) and the second stage of low current density (-1.35 mA cm<sup>-2</sup> / -1.45 mA cm<sup>-2</sup>). The bath solution contained CuSO<sub>4</sub>·5H<sub>2</sub>O (98%, Sigma-Aldrich, ACS reagent) 23 mM, ZnSO<sub>4</sub>·5H<sub>2</sub>O (99%, Sigma-Aldrich, ACS reagent) 34 mM, SnCl<sub>2</sub> (98%, Sigma-Aldrich, reagent grade) 16 mM, sodium citrate tribasic dehydrate 500 mM (99%, Sigma-Aldrich, ACS reagent) in deionized water.

And the as-deposited films were annealed in two-zone tubular furnace under S/Se atmosphere (200 sccm of 1 v/v% H<sub>2</sub>S/Ar gas, and Se gas evaporated from 400 °C of elemental Se). The films were heated from 100 °C to 550 °C with the heating rate of 5 °C/sec. The annealed films were immersed in 1 M KCN solution for 1 min to eliminate secondary phases.

### 3.1.3 Buffer, Window and Front Contact

Cadmium sulfide buffer layer was deposited using conventional chemical bath

deposition (CBD) method (at 60 °C, 10 min). Then intrinsic zinc oxide (i-ZnO) and aluminum-doped zinc oxide (AZO) was deposited by RF magnetron sputtering, and Ni/Al front contact was deposited sequentially by thermal evaporation. These sequences are described in Figure 3.1.1

## 3.2 Characterization

Efficiency of the CZTSSe solar cells were measured by a CHI608C potentiostat (CH Instrument) and a PEC-L11 solar simulator (Pecell Technologies) under AM1.5 1 Sun illumination condition which is calibrated with 91150V reference cell and meter (Newport). External quantum efficiency (EQE) of the devices were measured by G1218A Incident photon to current conversion efficiency system (PV Measurements). Short circuit current was also calculated from standard solar spectra (ASTM G173-03). Phases of the films were investigated using New D8 Advance X-ray diffractometer (XRD, Bruker) equipped with  $\text{CuK}\alpha$  ( $\lambda = 1.5418 \text{ \AA}$ ) X-ray. Morphology of the films were observed by scanning electron microscope (SEM, ZEISS, model MERLIN Compact). High-resolution transmission electron microscope (HR-TEM) image and selected area electron diffraction (SAED) patterns of the CZTSSe were taken from JEM-2100F (JEOL) and Tecnai F20 (FEI). Particle size distribution and fast Fourier transformation (FFT) were done by imageJ. Surface roughness information of the films was investigated with NX10 atomic force microscope (AFM, Park Systems). Transient photovoltage decay (TPVD) was

measured by MDO3000 oscilloscope (Tektronix) with white MWWHLP1 LED lamp (Thorlab) as a light bias and 405 nm iBeam smart 405-S-HP pulsed laser (Toptica) as an excitation light. Open circuit voltage – temperature plot (VOC – T plot) was measured by ZENNIUM potentiostat (ZAHNER) with LTS420E-P temperature controlled stage (Linkam).

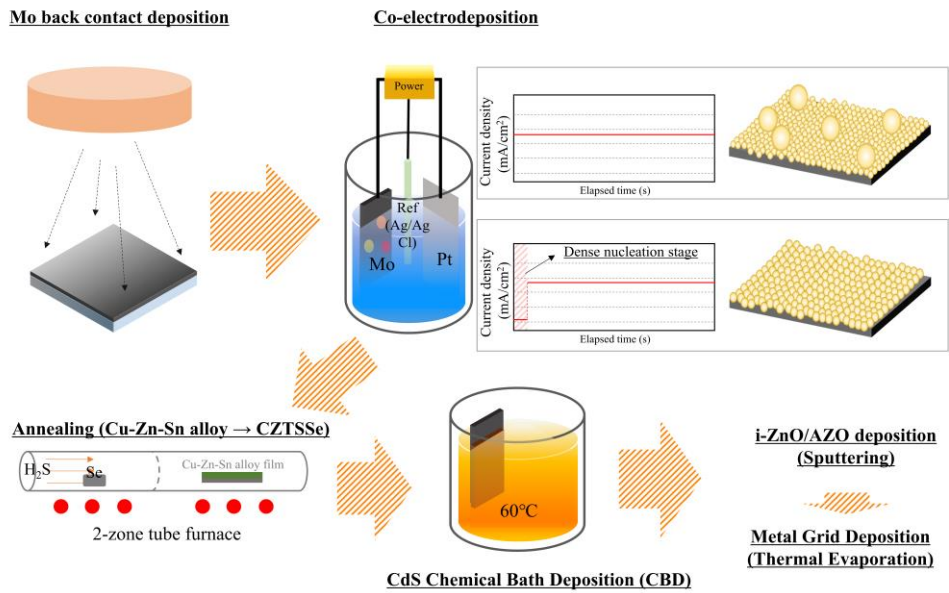


**Figure 3.1.1** Schemes of the fabrication process in this experiment.

## Chapter 4. Results and Discussion

### 4.1 Materials Characterization

Figure 4.1.1(a) ~ (d) shows the images of the as-deposited films after co-electrodeposition varying the operation time of nucleation stage ( $t_i = 0$  s, 10 s, 20 s, 30 s). At  $t_i = 0$  s condition (Fig. 1a), the film presented lots of abnormally grown large bumps (about 1  $\mu\text{m}$ ). As increasing  $t_i$ , it has been observed that the size of bumps became small and the particle size became uniform. Over 20 s, however, hydrogen evolution started on the Mo surface (Figure 4.1.2), which deteriorate the film uniformity.

CZTSSe after annealing process is presented in Fig. 4.1.1(e) ~ (h). The thickness of the films were about 1.3  $\mu\text{m}$ . As  $t_i$  increases, it was observed that the film became more flattened and uniform, which was also observed in the as-deposited case. Popped-out protrusions and dented voids disappeared as introducing initial stage. This would be beneficial to increasing shunt resistance since the voids can work as potential shunt path.

Figure 4.1.3 shows the histogram of particle size (in area) distribution estimated from SEM images. As we modified the nucleation stage, it was observed that the outliers, or abnormally grown bumps, disappeared. And this suppressed growth of abnormal dendritic bumps contributed to the reducing the roughness of the film.

The surface morphology and roughness of the films were investigated with AFM measurement. The three-dimensional reconstructed AFM images are depicted in Figure 4.1.4(a). It is observed that the dendritic protrusion in as-deposited alloy films became smaller as initial time increased, which is also observed in SEM. For annealed CZTSSe, films also became flattened as manipulating the nucleation step. We've calculated the quantitative values of the roughness. The root-mean-square roughness ( $R_{rms}$ ) data is plotted versus  $t_i$  in Figure 4.1.4(b). We could have observed that  $R_{rms}$  of the films decreased as  $t_i$  increased.  $R_{rms}$  of the as-deposited film decreased from  $0.121 \mu\text{m}$  ( $t_i = 0 \text{ s}$ ) to  $0.068 \mu\text{m}$  ( $t_i = 20 \text{ s}$ ) (-43.8%). Also,  $R_{rms}$  of the annealed CZTS films decreased from  $0.197 \mu\text{m}$  ( $t_i = 0 \text{ s}$ ) to  $0.140 \mu\text{m}$  ( $t_i = 20 \text{ s}$ ) (-28.9%). Deep dented voids are also observed at  $t_i = 0 \text{ s}$  condition. This can work as shunt path. Those voids became shallow at  $t_i = 20 \text{ s}$  condition, which is consistent with the images observed from SEM.

We've investigated the mechanism of dendritic growth of co-electrodeposited film. Figure 4.1.5(a) shows the voltage profile of galvanostatic co-electrodeposition. At stage A, Cu-rich Cu-Sn alloy start to be deposited on Mo and it shows very dense nucleation behavior (Figure 4.1.6). At stage B, since Cu is mass transfer limited, relatively Sn-rich Cu-Sn alloy start to be deposited on Cu-rich alloy. You can see the nuclei in Fig. 4.1.5(b). Its nucleation behavior is very sparse compared to Cu-rich alloy. It grows with edged shape sparse nucleation, and this sparse and edged nucleus works as a seed for dendritic growth. In Figure 4.1.8, TEM images and EDS

elemental composition of each part in the film at stage B is presented. At stage C, Zn starts to be deposited. This sequential procedure is depicted on Figure 4.1.5(c). In contrast, in case of nucleation manipulated condition, nucleation was much denser compared to the not manipulated condition (Figure 4.1.7). This suggest the dendritic growth can be suppressed through applying high current density which makes denser nucleation of tin-rich alloy.

While the nucleation behavior and morphology were significantly changed, the compositional changes of the films depending on  $t_i$  were negligibly small (Table 4.1.1). The elemental composition of the films was measured using energy dispersive x-ray spectroscopy (EDS).  $[Cu] / ([Zn] + [Sn])$  of the CZTSSe films was 0.86 ( $t_i = 0$  s), 0.87 ( $t_i = 10$  s), 0.86 ( $t_i = 20$  s), 0.85 ( $t_i = 30$  s) for each case. And  $[Zn] / [Sn]$  was 0.99 ( $t_i = 0$  s), 0.99 ( $t_i = 10$  s), 1.02 ( $t_i = 20$  s), 1.04 ( $t_i = 30$  s). Adjusting electrical variables may affect strongly on the composition because the electrochemical properties such as standard reduction potential, charge transfer kinetics, and diffusion coefficient of the metal species are quite different. Nevertheless, those films showed little change in composition since we only manipulated the nucleation stage and the growth stage, much longer compared to the nucleation stage, was kept same.

Crystallographic information of the films was investigated with XRD diffractometer (Figure 4.1.9). The XRD patterns of as-deposited films are presented at Figure 4.1.9(a). They mainly consist of the same 3 phases:  $Cu_6Sn_5$  (C 2/c, PDF

00-045-1488),  $\beta$ -Sn (I 4<sub>1</sub>/amd, PDF 04-004-7747), and Cu<sub>5</sub>Zn<sub>8</sub> (I $\bar{4}$ 3m, PDF 04-007-1117). From the fact that their diffraction patterns showed almost no difference in peak position or intensity, it is obvious that modified nucleation step didn't affect much on the crystal structure or phase fraction of the deposited films. The XRD patterns of CZTSSe films are presented at Figure 4.1.9(b). These patterns also show that there are almost no changes of the phases, composed of the kesterite CZTSSe phase (I $\bar{4}$ , PDF 04-019-1849) and small amount of zinc-rich secondary phase (ZnSe<sub>0.53</sub>S<sub>0.47</sub>, PDF 04-017-5149). Zn-rich secondary phase is detected by the peak near  $2\theta = 28^\circ$ . There was an appearance of MoS<sub>2</sub> peak at  $t_i = 20$  s,  $t_i = 30$  s condition. This abrupt increase of MoS<sub>2</sub> peak came from two-dimensional nature of MoS<sub>2</sub> film rather than physical increase of thickness or amount of it, considering that the thickness of MoS<sub>2</sub> didn't changed significantly (Figure 4.1.10) and also it was almost not detected in grazing incidence mode (Figure 4.1.11).

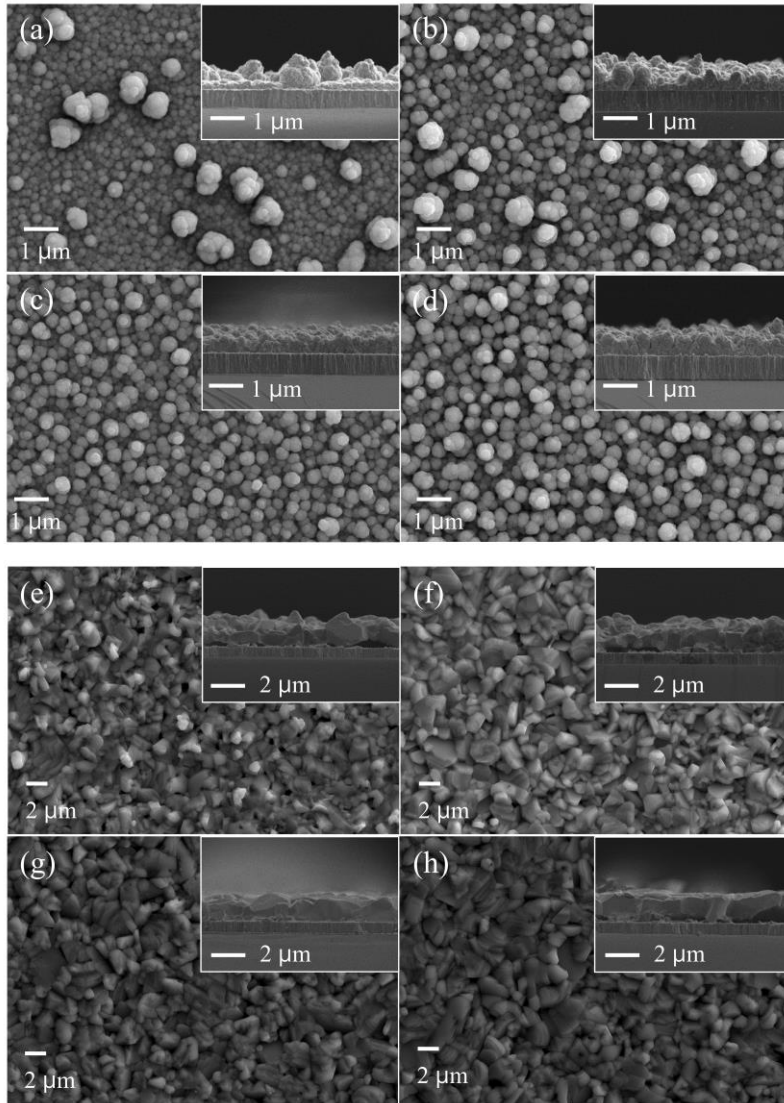


**Figure 4.1.1** (a) ~ (d) SEM images of as-deposited CZT alloy films on the Mo substrate depending on the operation time of initial stage,  $t_i$ . (a)  $t_i = 0$  s. (b)  $t_i = 10$  s. (c)  $t_i = 20$  s. (d)  $t_i = 30$  s. (e) ~ (h) SEM images of CZTSSe films on the Mo substrate depending on  $t_i$ . (e)  $t_i = 0$  s. (f)  $t_i = 10$  s. (g)  $t_i = 20$  s. (h)  $t_i = 30$  s.

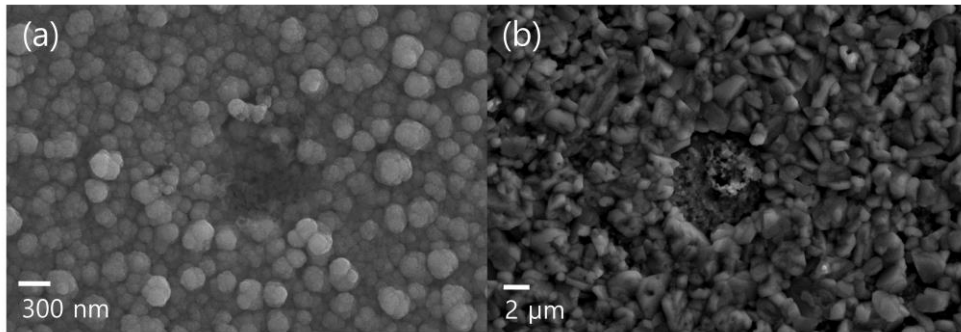


**Figure 4.1.2.** Fault at the film caused by hydrogen bubble. (at  $t_i = 30$  s condition) **(a)** as-deposited CZT alloy film, **(b)** CZTSSe films after annealing.

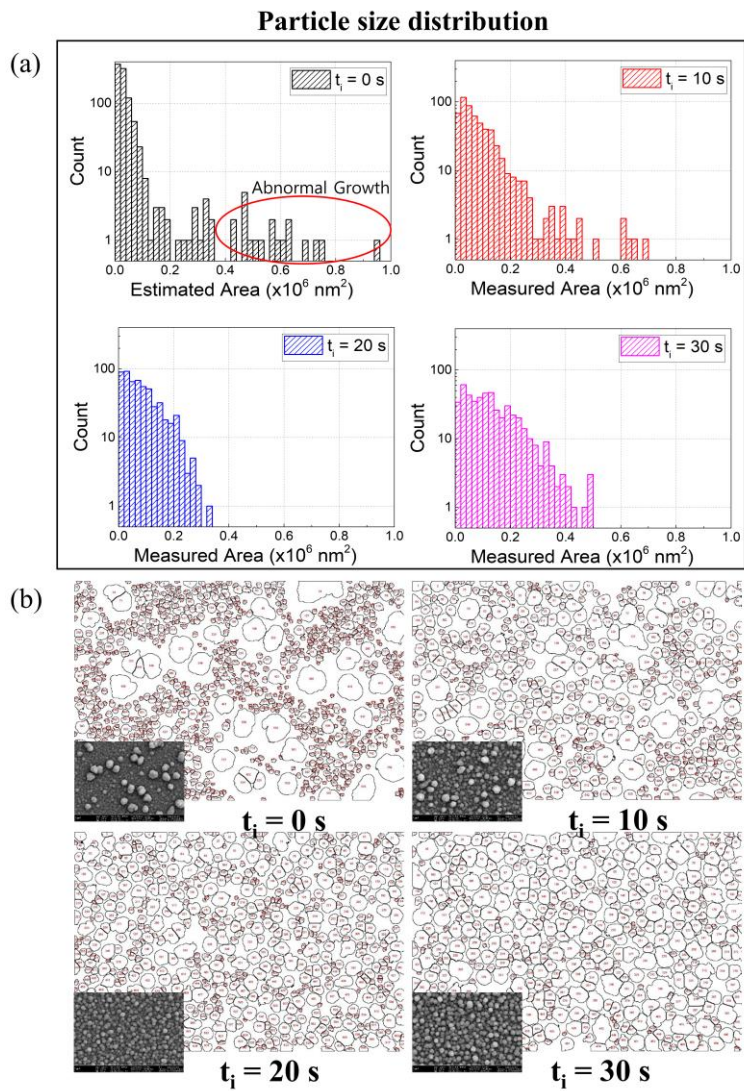


**Figure 4.1.3 (a)** Histogram of particle size distribution (in area) depending operation the time of initial stage ( $t_i$ ) (estimated from SEM images). Note that y-axis is presented in common log scale. **(b)** Corresponding particles processed from imageJ.

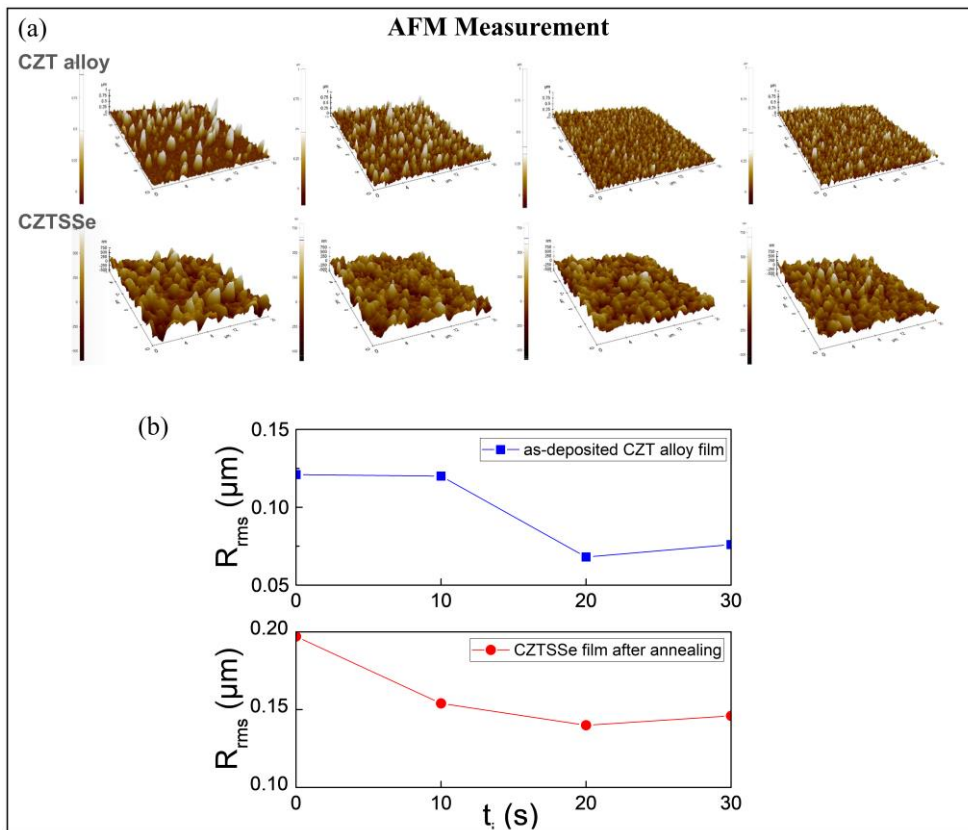


**Figure 4.1.4 (a)** AFM 3D reconstructed image ( $20\ \mu\text{m} \times 20\ \mu\text{m}$ ) and **(b)** Root-mean-square roughness ( $R_{rms}$ ) of the films depending on  $t_i$ . As-deposited CZT alloy film CZTSSe film after annealing process. In both cases, roughness was decreased as  $t_i$  was increased.

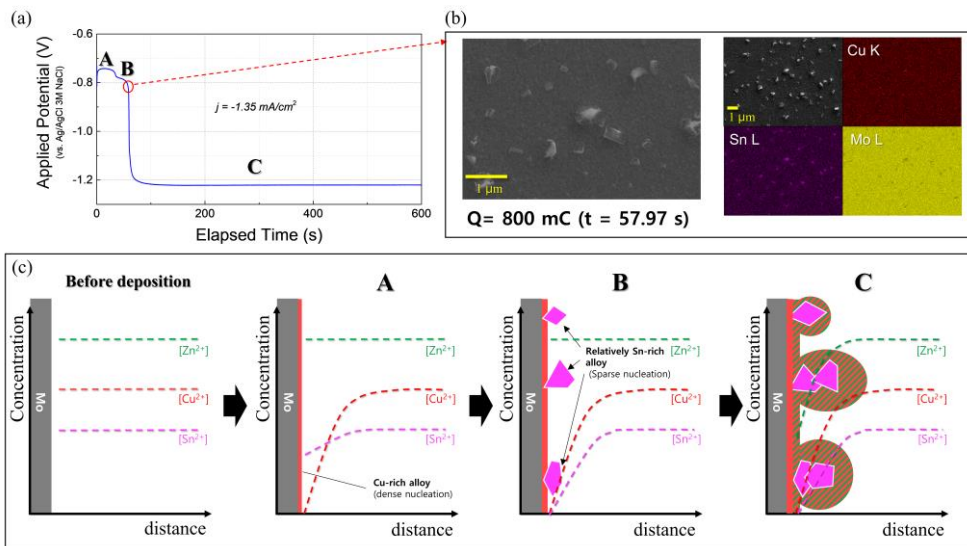


**Figure 4.1.5** (a) Voltage profile of conventional galvanostatic electrodeposition ( $t_i = 0$  s). (b) SEM images at  $t \approx 58$  s, and its corresponding EDS elemental mapping. (c) Schematic diagram describing the change in film morphology in sequence.

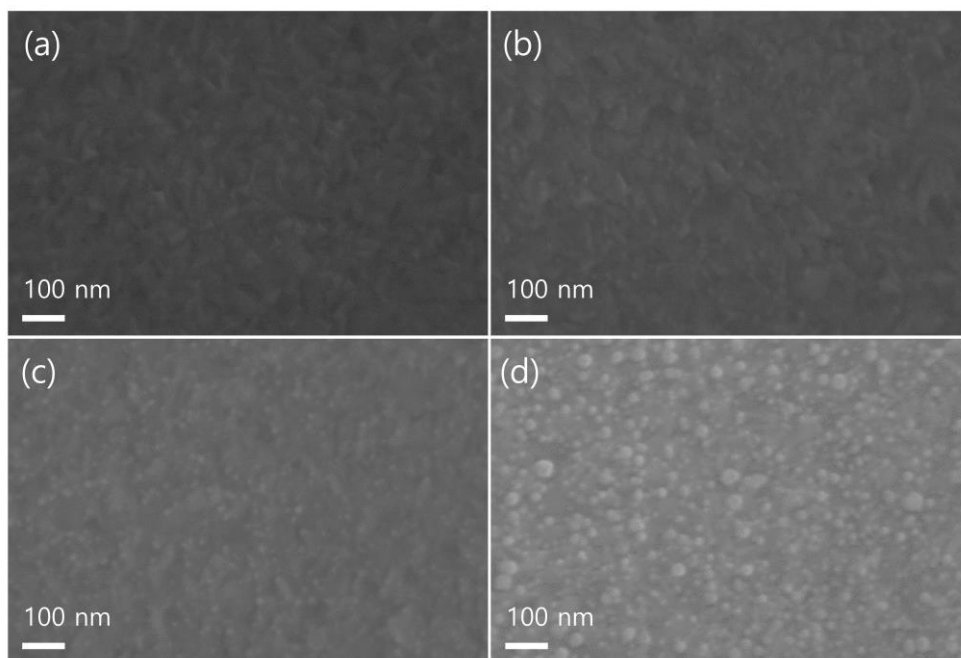


**Figure 4.1.6** Nucleation of Cu-Sn alloy under current density of  $-1.35\text{mA}/\text{cm}^2$ . **(a)**  $t = 0.5$  s, **(b)** 1.0 s, **(c)** 1.45 s, **(d)** 2.9 s.

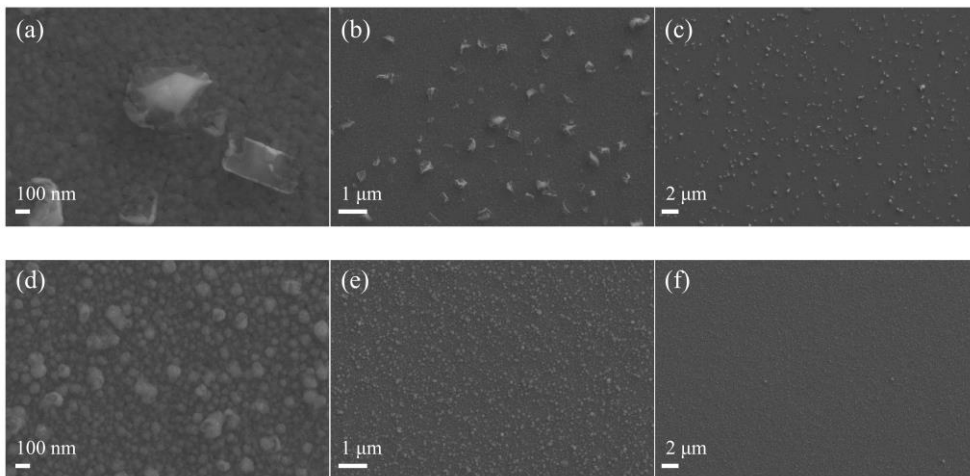


**Figure 4.1.7.** SEM images at total same charge of 800 mC ( $78.4 \text{ mC/cm}^2$ ). **(a) ~ (c)**  $-1.35 \text{ mA/cm}^2$  for 57.97 s. **(d) ~ (f)**  $-3.92 \text{ mA/cm}^2$  for 20 s.

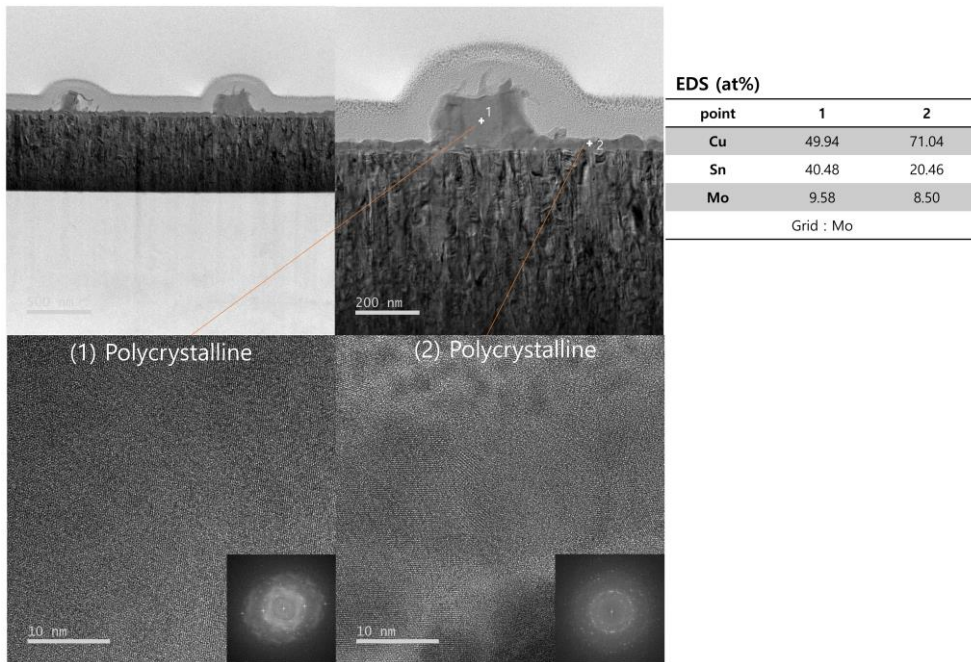


**Figure 4.1.8** TEM observation of deposited film at  $t = 57.97$  s ( $j = -1.35 \text{ mA/cm}^2$ ). The deposited alloy was partially polycrystalline. The stoichiometry of alloys can be inferred from the EDS measurements. Large nuclei is expected to be  $\text{Cu}_6\text{Sn}_5$ , and compact layer is expected to be  $\text{Cu}_3\text{Sn}$ .

Conditions	$t_i = 0$ s	$t_i = 10$ s	$t_i = 20$ s	$t_i = 30$ s	Note
[Cu] / ([Zn] + [Sn])	0.76 ± 0.01	0.72 ± 0.00	0.70 ± 0.01	0.70 ± 0.00	As-deposited alloy
	0.86 ± 0.01	0.87 ± 0.02	0.86 ± 0.01	0.85 ± 0.01	CZTSSe
[Zn] / [Sn]	0.92 ± 0.02	0.96 ± 0.01	0.95 ± 0.02	0.93 ± 0.00	As-deposited alloy
	0.99 ± 0.02	0.99 ± 0.03	1.02 ± 0.02	1.04 ± 0.02	CZTSSe
[S] / ([S] + [Se])	-	-	-	-	As-deposited alloy
	0.25 ± 0.00	0.25 ± 0.00	0.24 ± 0.00	0.25 ± 0.05	CZTSSe

**Table 4.1.1** Atomic composition of the films from EDS analysis.

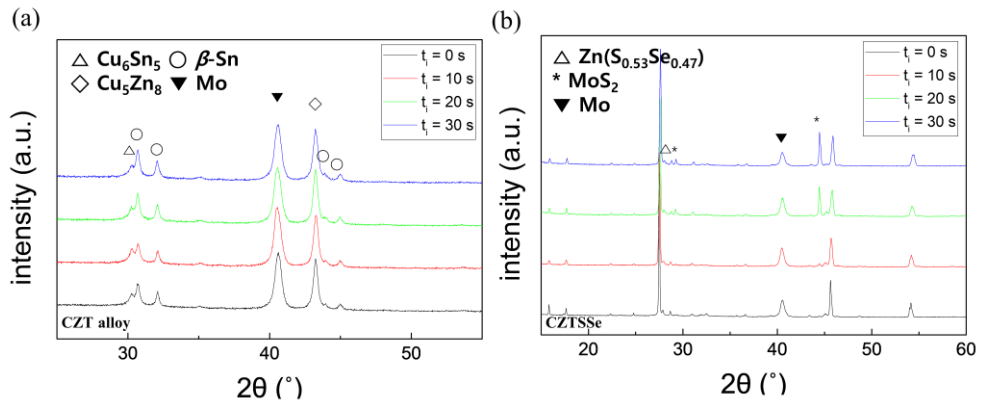


**Figure 4.1.9** XRD pattern of (a) as-deposited CZT alloy film and (b) annealed CZTSSe (coupled  $\theta$ - $2\theta$  scan).

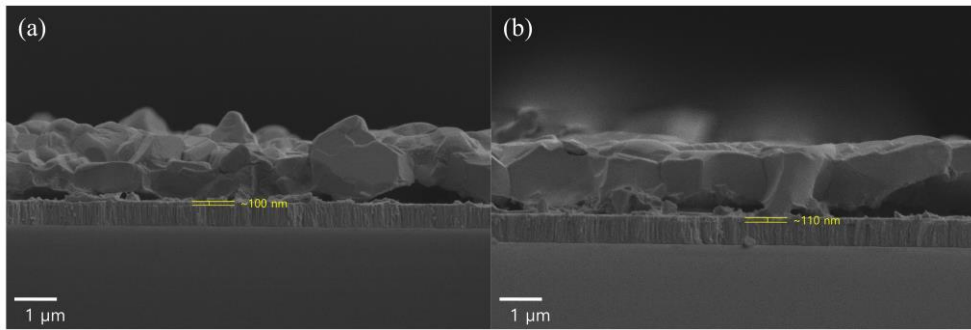


**Figure 4.1.10.** MoS<sub>2</sub> thickness of annealed CZTSSe films (a)  $t_i = 0$  s, (b)  $t_i = 30$  s.

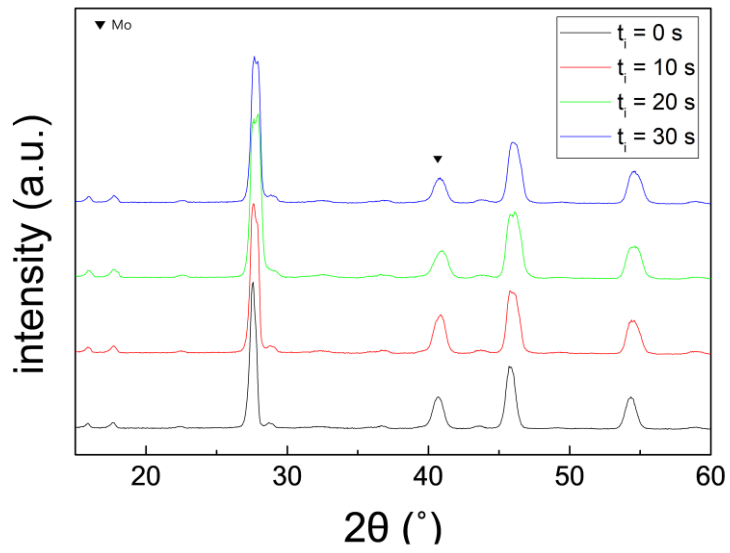


**Figure 4.1.11** GIXRD pattern of annealed CZTSSe films.

## 4.2 Device Characterization

Photovoltaic performances of the cells are presented on Figure 4.2.1. For appropriate representative, cells closed to the median value of power-conversion-efficiency (PCE) are compared at Figure 4.2.1(a).  $V_{OC}$  and fill factor were increased at roughness controlled condition ( $t_i = 20$  s). Diode parameters are also improved. Shunt conductance ( $G_{sh}$ ) and series resistance ( $R_s$ ) are decreased which leads to higher fill factor and better device performance. Statistical distribution of diode parameters estimated from dark J-V measurements are presented on Figure 4.2.2. Possible reason of the decrease in shunt conductance came from the disappearance of dented voids, which works as potential shunt path as mentioned before. This disappearance of voids can also contribute to low dark saturation current density, i.e. well-rectifying diode.

EQE spectra of these cells are presented at the Figure 4.2.1(b). They showed not significant difference through wide range of wavelength. Efficiency at infrared region was relatively small. This seems to come from not fully optimized thickness of the CZTSSe film (which is usually over  $2 \mu\text{m}$ ) considering that the photons of long wavelength have long penetration depth. Band gap calculated from the EQE spectra was about 1.17 eV. (Figure 4.2.3)

The relationship of improved device performance and roughness reduction can be also explained by reduced interface recombination. The rough surface morphology

makes larger interface area. Considering CZTSSe/CdS heterojunction interface is predominant recombination site [15, 60], larger interface area can lead to higher recombination rate [130]. This can be examined from the transient photovoltage decay (TPVD) measurements, which observe the decaying speed of the open circuit voltage when the light turned off. The carrier lifetime values from TPVD measurements,  $\tau_{TPVD}$ , are presented in Figure 4.2.4(a). Roughness controlled cell showed longer  $\tau_{TPVD}$  compared to the other one at same  $V_{OC}$ . It indicates that the recombination process is suppressed from the reduced interface area as mentioned above. Suppressed recombination in morphology controlled condition has contributed to higher  $V_{OC}$  and Fill Factor.

$V_{OC} - T$  plot also informs us dominant place where the recombination occurs. The relationship of  $V_{OC}$  and Temperature is given as [140]

$$V_{OC} \approx \frac{E_a}{q} - \frac{nkT}{q} \ln \left( \frac{J_{00}}{J_{SC}} \right)$$

Where  $E_a$  is an activation energy,  $q$  is an elementary charge,  $n$  is an ideality factor,  $k$  is Boltzmann constant,  $T$  is temperature,  $J_{00}$  is a reference current density and  $J_{SC}$  is a short circuit current density. This equation implies the linear relation between  $V_{OC}$  and  $T$ . The linear relationship holds true if only assuming the other parameters such as ideality factor ( $n$ ) are independent on the temperature, which doesn't hold true for CZTSSe. Still, the extrapolated y-intercept from the linear region has meaning of activation energy ( $E_a$ ). The activation energy is an index of determining

the place recombination occurs predominantly. When the bulk (space charge region or quasi neutral region) recombination is dominant, activation energy approaches to band gap energy ( $E_g$ ). When the interface recombination is dominant, however, activation energy  $E_a$  approaches to the barrier height ( $\Phi_b^p$ , Figure 4.2.5), which is much smaller than  $E_g$  [140-144].  $V_{OC} - T$  plot of the fabricated cells are presented on Figure 4.2.4(b). The flattened cell showed increased  $E_a$  by 80 mV compared to the rough one. This suggest that the interface recombination is suppressed as the interface area, which is predominant recombination site, has decreased.

The best cell efficiency of the cell was 8.63% of 0.39454 cm<sup>2</sup> active area. (Figure 4.2.6(a)) Statistically,  $J_{SC}$  was not improved much, and even decreased for the best cells. Reduced light trapping effect from the rough surface might be the possible reason. But it is clear that  $V_{OC}$  and fill factor were improved from reduced interface recombination also for the best cells. TEM observation of the roughness controlled ( $t_i = 20$  s) solar cell is presented on Figure 4.2.6(b) ~ (e). Figure 4.2.6(a) shows HAADF images of the CZTSSe cell. From the magnified image near the interface (Figure 4.2.6(c)), the thickness of CdS and i-ZnO is estimated as 45 nm and 60 nm for each. And the EDS line profile (Figure 4.2.6(d)) of the film clarified that cations were well distributed evenly over the film. SAED pattern of the bulk CZTSSe is presented on Fig. 4.2.6(e).  $\langle 221 \rangle$  zone axis could be inferred from the diffraction symmetry.  $d$ -spacing of each plane could be inferred from the SAED pattern (Fig. 4.2.7).  $d_{110} = 0.41$  nm,  $d_{204} = 0.20$  nm, and  $d_{114} = 0.23$  nm. Which is consistent with

d-spacing from the XRD data ( $d_{110} = 0.3961$  nm,  $d_{204} = 0.1978$  nm,  $d_{114} = 0.2283$  nm). Zn-rich secondary phase was observed from elemental mapping of EDS measurements (Figure 4.2.9), which is consistent with the XRD measurements. Total distribution of experimented data is presented on Figure 4.2.10.

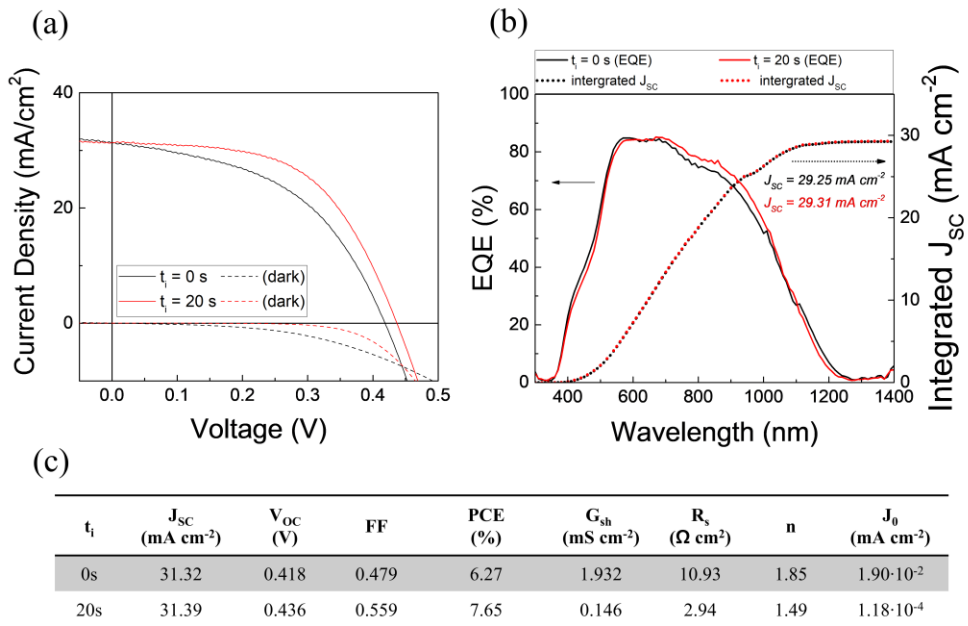


**Figure 4.2.1 (a)~(c)** Device characteristics of cells close to the median value depending on  $t_i$ . ((a) J-V measurement (b) EQE spectra (c) Device parameters)

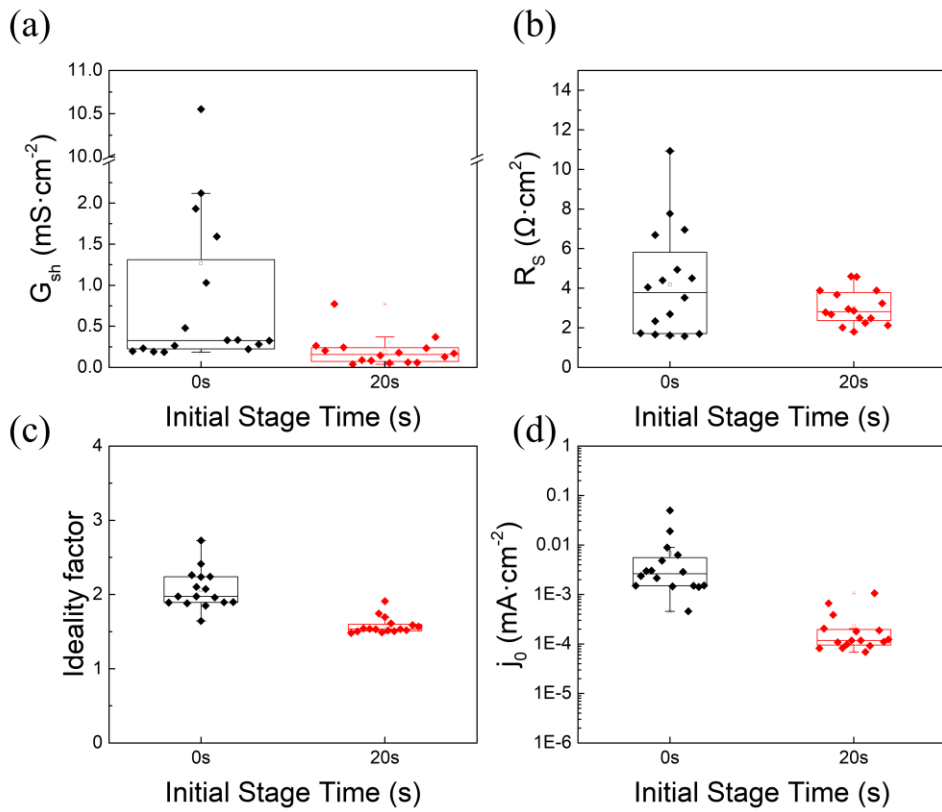


**Figure 4.2.2** Statistical box plots of diode parameters depending on  $t_i = 0s$ . ((a) Shunt conductance (b) Series resistance (c) Ideality factor (d) Dark saturation current.)

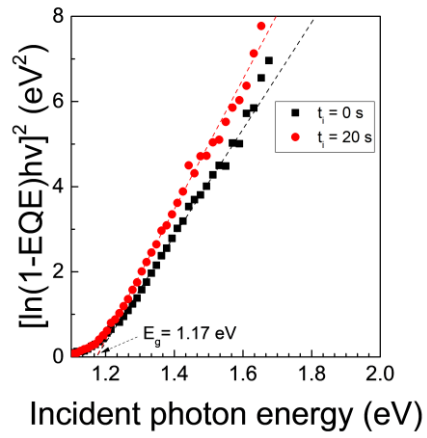


**Figure 4.2.3** Band gap energy estimated from the measured EQE spectra.

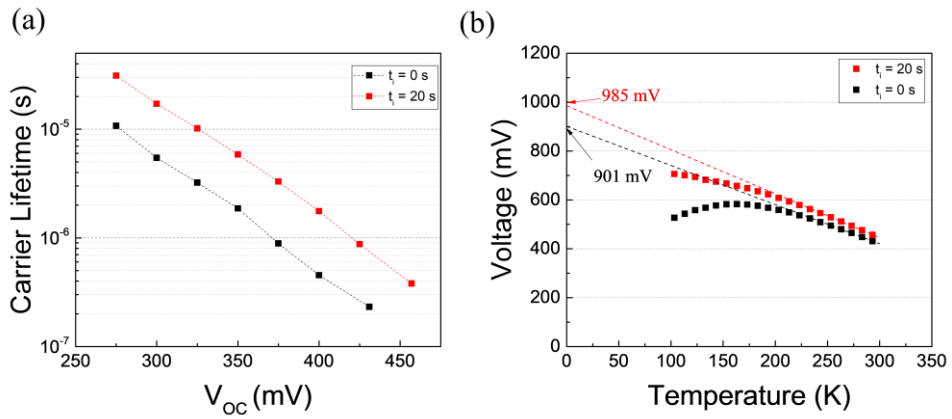


**Figure 4.2.4** Carrier lifetime measured from transient photovoltage decay (b)  $V_{OC}$  measured at different temperature points and activation energy ( $E_a$ ) estimated from extrapolation.

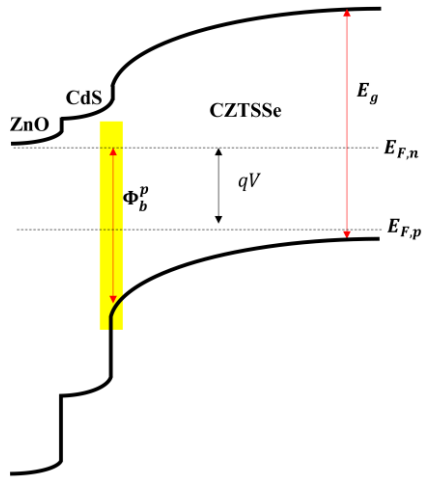


**Figure 4.2.5** Schematic band diagram of CZTSSe solar cell.

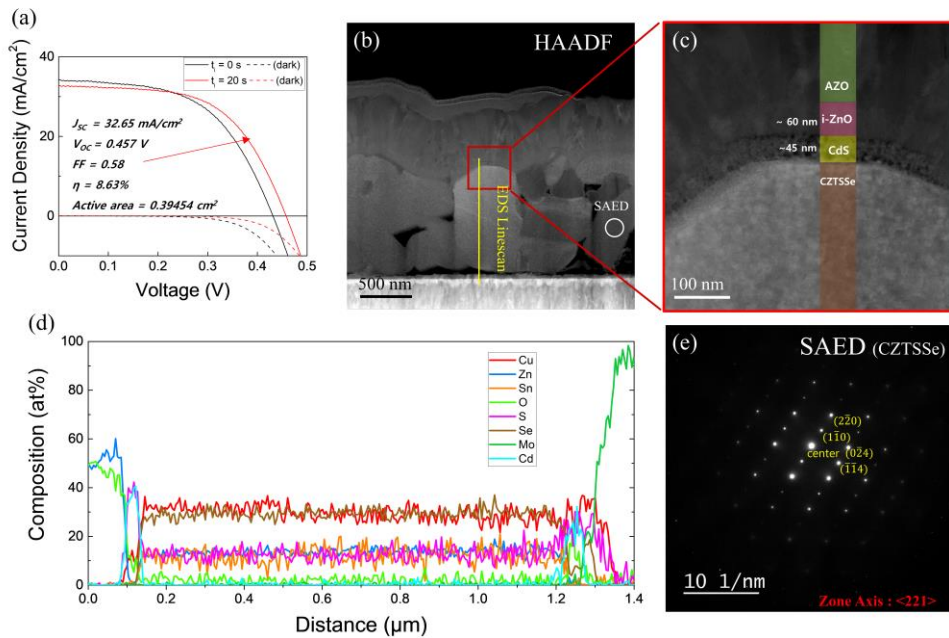


**Figure 4.2.6** (a) Best performing cells at each condition. (b) ~ (e) TEM observation of the device. (b) HAADF image of cross-sectional view. (c) CZTSSe/CdS interface. (d) EDS Line profile of elements. (e) Electron diffraction pattern.

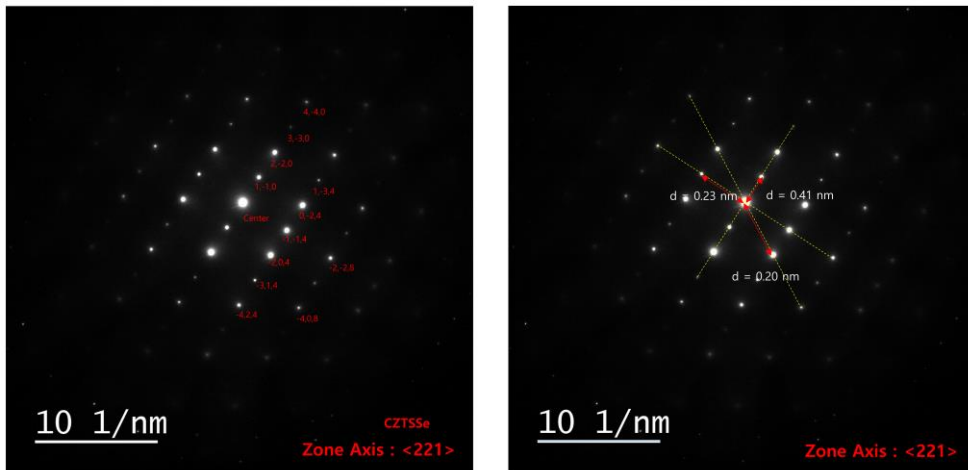


**Figure 4.2.7** SAED pattern of CZTSSe. Plane indices and their corresponding  $d$ -spacing.

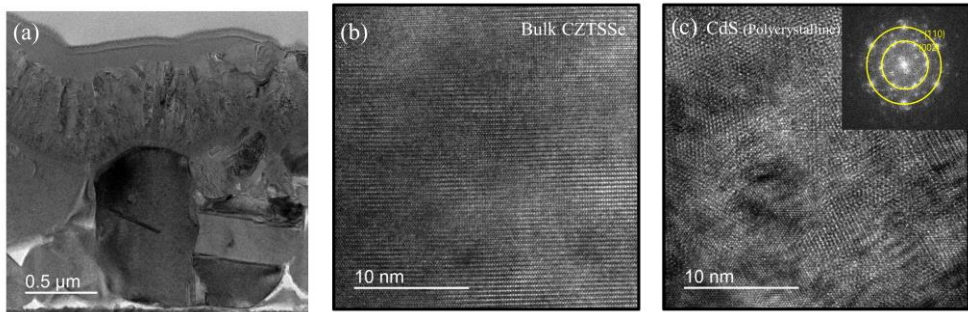


**Figure 4.2.8 (a) ~ (c)** Bright field TEM images of the device. **(b)** HR image at bulk CZTSSe **(c)** polycrystalline CdS.

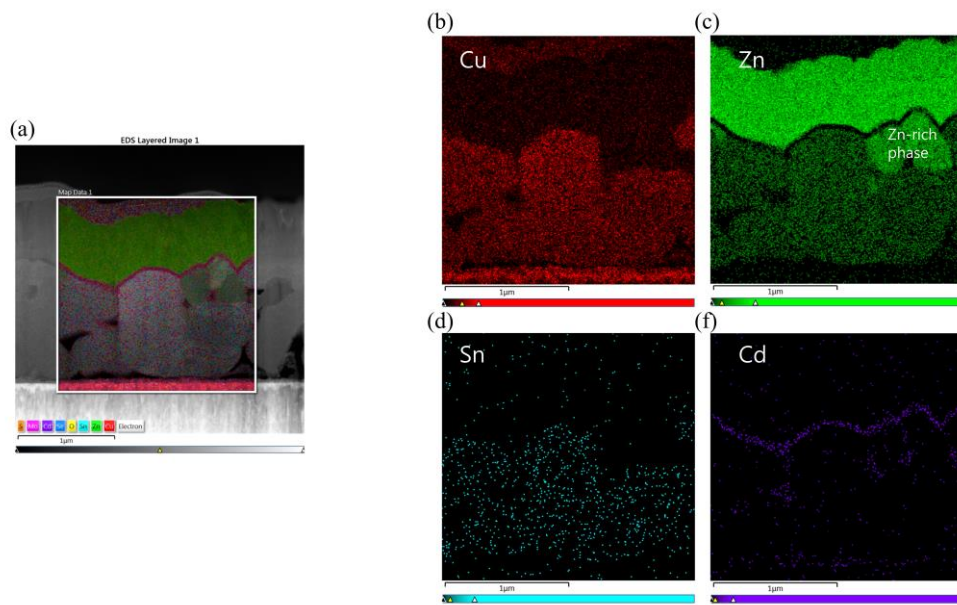


**Figure 4.2.9** EDS mapping of the crosssection. **(a)** Integrated image, signals of **(b)** Cu **(c)** Zn **(d)** Sn **(f)** Cd.

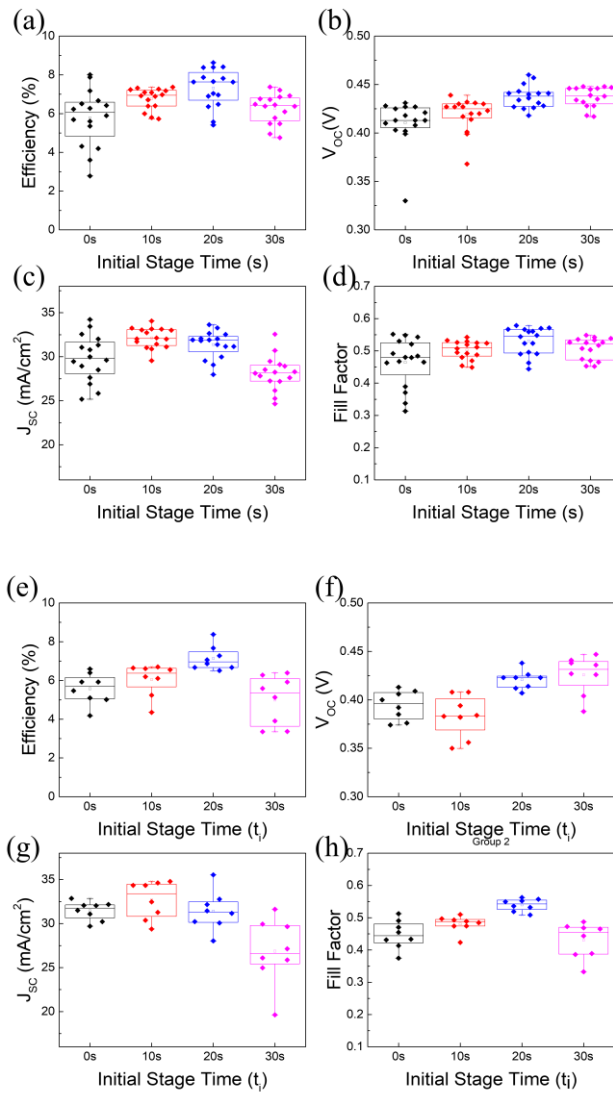


**Figure 4.2.10** Statistical box plots of cell performances and factors depending on  $t_i = (0\text{ s}, 10\text{ s}, 20\text{ s}, 30\text{ s})$ . **(a) ~ (d)** Applied current density:  $-3.92\text{ mA cm}^{-2} / -1.45\text{ mA cm}^{-2}$  **(e) ~ (h)** Applied current density:  $-3.92\text{ mA cm}^{-2} / -1.35\text{ mA cm}^{-2}$  for each stage. (1<sup>st</sup>/2<sup>nd</sup>)

## Chapter 5. Conclusions

We've fabricated CZTSSe solar cells with galvanostatic co-electrodeposition method. As applying high current density at nucleation stage, we've manipulated the morphology and roughness of the CZT alloy and CZTSSe absorber layer film with little elemental composition change. The roughness reduction can be observed by SEM and AFM, and the quantitative value of the roughness ( $R_{rms}$ ) has decreased (CZT alloy: -43.8% / CZTSSe: -29.8%). Their size distribution showed that the abnormal dendritic growth, which was caused from sparse nucleation of tin-rich alloy, was suppressed. Flattened morphology has contributed to improved device performance, 8.63% at best of 0.39454 cm<sup>2</sup> active area.  $\tau_{TPVD}$  of roughness controlled cell was several times longer than not controlled one, suggesting reduced recombination. Activation energy from the VOC – T plot also increased, which also implies that the interface recombination was suppressed compared to the reference. In short, we controlled the morphology and roughness of CZTSSe solar cell through electrochemically manipulating the nucleation stage. And this approach was beneficial improve  $V_{OC}$  and fill factor by suppressing interface recombination. Additional nucleation optimization or thickness optimization is expected for the further improvement.

## Bibliography

- [1] J. Goldemberg, 《 *World Energy Assessment: Energy and the challenge of sustainability* 》, **2000**, United Nations Development Programme New York^ eNY NY.
- [2] BP, 《 *Statistical Review of World Energy 67th Ed : Renewable Energy* 》, **2018**.
- [3] P. Rappaport, *Solar Energy*, **1959**. 3(4): 8-18.
- [4] W. Shockley and H.J. Queisser, *Journal of applied physics*, **1961**. 32(3): 510-519.
- [5] S. Rühle, *Solar Energy*, **2016**. 130: 139-147.
- [6] A. Polman, M. Knight, E.C. Garnett, B. Ehrler, and W.C. Sinke, *Science*, **2016**. 352(6283): aad4424.
- [7] A. Goetzberger, C. Hebling, and H.-W. Schock, *Materials Science and Engineering: R: Reports*, **2003**. 40(1): 1-46.
- [8] J. Ramanujam and U.P. Singh, *Energy & Environmental Science*, **2017**. 10(6): 1306-1319.
- [9] M. Aman, K. Solangi, M. Hossain, A. Badarudin, G. Jasmon, H. Mokhlis, A. Bakar, and S. Kazi, *Renewable and Sustainable Energy Reviews*, **2015**. 41: 1190-1204.
- [10] B.E. Hardin, H.J. Snaith, and M.D. McGehee, *Nature photonics*, **2012**. 6(3): 162.
- [11] J.-P. Correa-Baena, A. Abate, M. Saliba, W. Tress, T.J. Jacobsson, M. Grätzel, and A. Hagfeldt, *Energy & Environmental Science*, **2017**. 10(3): 710-727.
- [12] H.J. Snaith, *Nature materials*, **2018**. 17(5): 372.
- [13] P. Cheng and X. Zhan, *Chemical Society Reviews*, **2016**. 45(9): 2544-2582.
- [14] G.H. Carey, A.L. Abdelhady, Z. Ning, S.M. Thon, O.M. Bakr, and E.H. Sargent, *Chemical reviews*, **2015**. 115(23): 12732-12763.
- [15] K. Kaur, N. Kumar, and M. Kumar, *Journal of Materials Chemistry A*, **2017**. 5(7): 3069-3090.
- [16] S.K. Wallace, D.B. Mitzi, and A. Walsh, *ACS Energy Letters*, **2017**. 2(4): 776-779.
- [17] A. Polizzotti, I.L. Repins, R. Noufi, S.-H. Wei, and D.B. Mitzi, *Energy & Environmental Science*, **2013**. 6(11): 3171-3182.
- [18] K. Ito and T. Nakazawa, *Japanese Journal of Applied Physics*, **1988**. 27(11R): 2094.
- [19] H. Katagiri, N. Sasaguchi, S. Hando, S. Hoshino, J. Ohashi, and T. Yokota, *Solar*

- Energy Materials and Solar Cells*, **1997**. 49(1-4): 407-414.
- [20] D.A.R. Barkhouse, O. Gunawan, T. Gokmen, T.K. Todorov, and D.B. Mitzi, *Progress in Photovoltaics: Research and Applications*, **2012**. 20(1): 6-11.
- [21] T.K. Todorov, K.B. Reuter, and D.B. Mitzi, *Advanced materials*, **2010**. 22(20): E156-E159.
- [22] T.K. Todorov, J. Tang, S. Bag, O. Gunawan, T. Gokmen, Y. Zhu, and D.B. Mitzi, *Advanced Energy Materials*, **2013**. 3(1): 34-38.
- [23] W. Wang, M.T. Winkler, O. Gunawan, T. Gokmen, T.K. Todorov, Y. Zhu, and D.B. Mitzi, *Advanced Energy Materials*, **2014**. 4(7): 5.
- [24] S. Ahn, S. Jung, J. Gwak, A. Cho, K. Shin, K. Yoon, D. Park, H. Cheong, and J.H. Yun, *Applied Physics Letters*, **2010**. 97(2): 021905.
- [25] S. Chen, A. Walsh, J.-H. Yang, X.-G. Gong, L. Sun, P.-X. Yang, J.-H. Chu, and S.-H. Wei, *Physical Review B*, **2011**. 83(12): 125201.
- [26] C. Persson, *Journal of Applied Physics*, **2010**. 107(5): 053710.
- [27] F. Liu, Y. Li, K. Zhang, B. Wang, C. Yan, Y. Lai, Z. Zhang, J. Li, and Y. Liu, *Solar Energy Materials and Solar Cells*, **2010**. 94(12): 2431-2434.
- [28] J.-S. Seol, S.-Y. Lee, J.-C. Lee, H.-D. Nam, and K.-H. Kim, *Solar Energy Materials and Solar Cells*, **2003**. 75(1-2): 155-162.
- [29] S. Chen, J.-H. Yang, X.-G. Gong, A. Walsh, and S.-H. Wei, *Physical Review B*, **2010**. 81(24): 245204.
- [30] S. Chen, L.-W. Wang, A. Walsh, X. Gong, and S.-H. Wei, *Applied Physics Letters*, **2012**. 101(22): 223901.
- [31] K. Ito, 《*Copper zinc tin sulfide-based thin-film solar cells*》, **2014**, John Wiley & Sons.
- [32] S. Chen, A. Walsh, X.G. Gong, and S.H. Wei, *Advanced Materials*, **2013**. 25(11): 1522-1539.
- [33] D. Han, Y. Sun, J. Bang, Y. Zhang, H.-B. Sun, X.-B. Li, and S. Zhang, *Physical Review B*, **2013**. 87(15): 155206.
- [34] M.J. Romero, H. Du, G. Teeter, Y. Yan, and M.M. Al-Jassim, *Physical Review B*, **2011**. 84(16): 165324.
- [35] B.I. Shklovskii and A.L. Efros, 《*Electronic properties of doped semiconductors*》,

Vol. 45, **2013**, Springer Science & Business Media.

- [36] D. Shin, B. Saparov, and D.B. Mitzi, *Advanced Energy Materials*, **2017**. 7(11): 1602366.
- [37] H.M. Branz and M. Silver, *Physical Review B*, **1990**. 42(12): 7420.
- [38] Y. Bar-Yam, D. Adler, and J. Joannopoulos, *Physical review letters*, **1986**. 57(4): 467.
- [39] G. Borghs, K. Bhattacharyya, K. Deneffe, P. Van Mieghem, and R. Mertens, *Journal of applied physics*, **1989**. 66(9): 4381-4386.
- [40] I. Dirnstorfer, M. Wagner, D.M. Hofmann, M. Lampert, F. Karg, and B.K. Meyer, *physica status solidi (a)*, **1998**. 168(1): 163-175.
- [41] T. Gokmen, O. Gunawan, T.K. Todorov, and D.B. Mitzi, *Applied Physics Letters*, **2013**. 103(10): 103506.
- [42] S. Bourdais, C. Choné, B. Delatouche, A. Jacob, G. Larramona, C. Moisan, A. Lafond, F. Donatini, G. Rey, and S. Siebentritt, *Advanced Energy Materials*, **2016**. 6(12): 1502276.
- [43] J. Leitao, N.M. Santos, P. Fernandes, P. Salome, A. Da Cunha, J. González, G. Ribeiro, and F. Martinaga, *Physical Review B*, **2011**. 84(2): 024120.
- [44] H.-R. Liu, S. Chen, Y.-T. Zhai, H.-J. Xiang, X.-G. Gong, and S.-H. Wei, *Journal of Applied Physics*, **2012**. 112(9): 093717.
- [45] M. Kumar, A. Dubey, N. Adhikari, S. Venkatesan, and Q. Qiao, *Energy & Environmental Science*, **2015**. 8(11): 3134-3159.
- [46] Y. Hashimoto, N. Kohara, T. Negami, M. Nishitani, and T. Wada, *Japanese journal of applied physics*, **1996**. 35(9R): 4760.
- [47] S. Niki, P. Fons, A. Yamada, Y. Lacroix, H. Shibata, H. Oyanagi, M. Nishitani, T. Negami, and T. Wada, *Applied physics letters*, **1999**. 74(11): 1630-1632.
- [48] M. Weber, R. Scheer, H. Lewerenz, H. Jungblut, and U. Störkel, *Journal of The Electrochemical Society*, **2002**. 149(1): G77-G84.
- [49] M. Buffiere, G. Brammertz, S. Sahayaraj, M. Batuk, S. Khelifi, D. Mangin, A.A. El Mel, L. Arzel, J. Hadermann, M. Meuris, and J. Poortmans, *Acs Applied Materials & Interfaces*, **2015**. 7(27): 14690-14698.
- [50] A. Fairbrother, E. Garcia-Hemme, V. Izquierdo-Roca, X. Fontane, F.A. Pulgarin-

- Agudelo, O. Vigil-Galan, A. Perez-Rodriguez, and E. Saucedo, *Journal of the American Chemical Society*, **2012**. 134(19): 8018-8021.
- [51] H. Xie, Y. Sánchez, S.n. López-Marino, M.s. Espíndola-Rodríguez, M. Neuschitzer, D. Sylla, A. Fairbrother, V. Izquierdo-Roca, A. Pérez-Rodríguez, and E. Saucedo, *ACS applied materials & interfaces*, **2014**. 6(15): 12744-12751.
- [52] A. Chavda, M. Patel, I. Mukhopadhyay, and A. Ray, *ACS Sustainable Chemistry & Engineering*, **2016**. 4(4): 2302-2308.
- [53] W. Wang, G. Chen, H. Cai, B. Chen, L. Yao, M. Yang, S. Chen, and Z. Huang, *Journal of Materials Chemistry A*, **2018**. 6(7): 2995-3004.
- [54] S. Hall, J. Szymanski, and J. Stewart, *The Canadian Mineralogist*, **1978**. 16(2): 131-137.
- [55] K. Yu and E.A. Carter, *Chemistry of Materials*, **2015**. 27(8): 2920-2927.
- [56] X. Lu, Z. Zhuang, Q. Peng, and Y. Li, *Chemical Communications*, **2011**. 47(11): 3141-3143.
- [57] J. Paier, R. Asahi, A. Nagoya, and G. Kresse, *Physical Review B*, **2009**. 79(11): 115126.
- [58] S. Schorr, H.-J. Hoebler, and M. Tovar, *European Journal of Mineralogy*, **2007**. 19(1): 65-73.
- [59] A. Singh, H. Geaney, F. Laffir, and K.M. Ryan, *Journal of the American Chemical Society*, **2012**. 134(6): 2910-2913.
- [60] K. Wang, O. Gunawan, T. Todorov, B. Shin, S. Chey, N. Bojarczuk, D. Mitzi, and S. Guha, *Applied Physics Letters*, **2010**. 97(14): 143508.
- [61] J.J. Scragg, J.T. Watjen, M. Edoff, T. Ericson, T. Kubart, and C. Platzer-Bjorkman, *Journal of the American Chemical Society*, **2012**. 134(47): 19330-19333.
- [62] B. Shin, Y. Zhu, N.A. Bojarczuk, S. Jay Chey, and S. Guha, *Applied Physics Letters*, **2012**. 101(5): 053903.
- [63] J.J. Scragg, T. Kubart, J.T. Wätjen, T. Ericson, M.K. Linnarsson, and C. Platzer-Björkman, *Chemistry of Materials*, **2013**. 25(15): 3162-3171.
- [64] S. López-Marino, M. Placidi, A. Pérez-Tomás, J. Llobet, V. Izquierdo-Roca, X. Fontané, A. Fairbrother, M. Espíndola-Rodríguez, D. Sylla, and A. Pérez-Rodríguez, *Journal of Materials Chemistry A*, **2013**. 1(29): 8338-8343.

- [65] F. Zhou, F. Zeng, X. Liu, F. Liu, N. Song, C. Yan, A. Pu, J. Park, K. Sun, and X. Hao, *ACS applied materials & interfaces*, **2015**. 7(41): 22868-22873.
- [66] P.D. Antunez, D.M. Bishop, Y. Luo, and R. Haight, *Nature Energy*, **2017**. 2(11): 884.
- [67] P.D. Antunez, D.M. Bishop, Y.S. Lee, T. Gokmen, O. Gunawan, T.S. Gershon, T.K. Todorov, S. Singh, and R. Haight, *Advanced Energy Materials*, **2017**. 7(15): 1602585.
- [68] M.T. Htay, Y. Hashimoto, N. Momose, K. Sasaki, H. Ishiguchi, S. Igarashi, K. Sakurai, and K. Ito, *Japanese Journal of Applied Physics*, **2011**. 50(3R): 032301.
- [69] M. Nguyen, K. Ernits, K.F. Tai, C.F. Ng, S.S. Pramana, W.A. Sasangka, S.K. Batabyal, T. Holopainen, D. Meissner, and A. Neisser, *Solar Energy*, **2015**. 111: 344-349.
- [70] T. Ericson, J.J. Scragg, A. Hultqvist, J.T. Watjen, P. Szaniawski, T. Torndahl, and C. Platzer-Bjorkman, *IEEE Journal of Photovoltaics*, **2014**. 4(1): 465-469.
- [71] T. Ericson, F. Larsson, T. Törndahl, C. Frisk, J. Larsen, V. Kosyak, C. Häggglund, S. Li, and C. Platzer-Björkman, *Solar RRL*, **2017**. 1(5): 1700001.
- [72] F. Jiang, C. Ozaki, T. Harada, Z. Tang, T. Minemoto, Y. Nose, and S. Ikeda, *Chemistry of Materials*, **2016**. 28(10): 3283-3291.
- [73] S. Siol, T.P. Dhakal, G.S. Gudavalli, P.P. Rajbhandari, C. DeHart, L.L. Baranowski, and A. Zakutayev, *ACS applied materials & interfaces*, **2016**. 8(22): 14004-14011.
- [74] D.A.R. Barkhouse, R. Haight, N. Sakai, H. Hiroi, H. Sugimoto, and D.B. Mitzi, *Applied Physics Letters*, **2012**. 100(19): 193904.
- [75] C. Yan, F. Liu, N. Song, B.K. Ng, J.A. Stride, A. Tadich, and X. Hao, *Applied Physics Letters*, **2014**. 104(17): 173901.
- [76] D.B. Mitzi, O. Gunawan, T.K. Todorov, K. Wang, and S. Guha, *Solar Energy Materials and Solar Cells*, **2011**. 95(6): 1421-1436.
- [77] C. Platzer-Björkman, C. Frisk, J. Larsen, T. Ericson, S.-Y. Li, J. Scragg, J. Keller, F. Larsson, and T. Törndahl, *Applied Physics Letters*, **2015**. 107(24): 243904.
- [78] S. Ishizuka, K. Sakurai, A. Yamada, K. Matsubara, P. Fons, K. Iwata, S. Nakamura, Y. Kimura, T. Baba, and H. Nakanishi, *Solar energy materials and solar cells*, **2005**. 87(1-4): 541-548.
- [79] R. Scheer, L. Messmann-Vera, R. Klenk, and H.W. Schock, *Progress in*

- Photovoltaics: Research and Applications*, **2012**. 20(6): 619-624.
- [80] Y.S. Lee, T. Gershon, T.K. Todorov, W. Wang, M.T. Winkler, M. Hopstaken, O. Gunawan, and J. Kim, *Advanced Energy Materials*, **2016**. 6(12): 5.
- [81] Y.S. Lee, T. Gershon, O. Gunawan, T.K. Todorov, T. Gokmen, Y. Virgus, and S. Guha, *Advanced Energy Materials*, **2015**. 5(7): 4.
- [82] S. Kim, K.M. Kim, H. Tampo, H. Shibata, and S. Niki, *Applied Physics Express*, **2016**. 9(10): 102301.
- [83] B. Shin, O. Gunawan, Y. Zhu, N.A. Bojarczuk, S.J. Chey, and S. Guha, *Progress in Photovoltaics: Research and Applications*, **2013**. 21(1): 72-76.
- [84] K.-J. Yang, D.-H. Son, S.-J. Sung, J.-H. Sim, Y.-I. Kim, S.-N. Park, D.-H. Jeon, J. Kim, D.-K. Hwang, and C.-W. Jeon, *Journal of Materials Chemistry A*, **2016**. 4(26): 10151-10158.
- [85] C. Yan, K. Sun, J. Huang, S. Johnston, F. Liu, B.P. Veettil, K. Sun, A. Pu, F. Zhou, and J.A. Stride, *ACS Energy Letters*, **2017**. 2(4): 930-936.
- [86] C. Yan, J. Huang, K. Sun, S. Johnston, Y. Zhang, H. Sun, A. Pu, M. He, F. Liu, K. Eder, L. Yang, J.M. Cairney, N.J. Ekins-Daukes, Z. Hameiri, J.A. Stride, S. Chen, M.A. Green, and X. Hao, *Nature Energy*, **2018**.
- [87] A. Nandur and B. White. in *APS Meeting Abstracts*. 2014.
- [88] X. Zeng, K.F. Tai, T. Zhang, C.W.J. Ho, X. Chen, A. Huan, T.C. Sum, and L.H. Wong, *Solar Energy Materials and Solar Cells*, **2014**. 124: 55-60.
- [89] A. Collord and H. Hillhouse, *Chemistry of Materials*, **2016**. 28(7): 2067-2073.
- [90] G. Larramona, S. Levchenko, S. Bourdais, A. Jacob, C. Choné, B. Delatouche, C. Moisan, J. Just, T. Unold, and G. Dennler, *Advanced Energy Materials*, **2015**. 5(24): 1501404.
- [91] L. Vauche, L. Risch, Y. Sánchez, M. Dimitrievska, M. Pasquinelli, T. Goislard de Monsabert, P.P. Grand, S. Jaime-Ferrer, and E. Saucedo, *Progress in Photovoltaics: Research and Applications*, **2016**. 24(1): 38-51.
- [92] S.W. Seo, J.O. Jeon, J.W. Seo, Y.Y. Yu, J.h. Jeong, D.K. Lee, H. Kim, M.J. Ko, H.J. Son, H.W. Jang, and J.Y. Kim, *ChemSusChem*, **2016**. 9(5): 439-444.
- [93] S.G. Haass, M. Diethelm, M. Werner, B. Bissig, Y.E. Romanyuk, and A.N. Tiwari, *Advanced Energy Materials*, **2015**. 5(18): 7.

- [94] X. Hao, K.J. K., B.I. L., and H.H. W., *Advanced Energy Materials*, **2014**. 4(11): 1301823.
- [95] H. Xin, S. Vorpahl, A. Collord, I. Braly, A. Uhl, B. Krueger, D. Ginger, and H. Hillhouse, *Physical Chemistry Chemical Physics*, **2015**. 17(37): 23859-23866.
- [96] Q. Guo, G.M. Ford, W.C. Yang, B.C. Walker, E.A. Stach, H.W. Hillhouse, and R. Agrawal, *Journal of the American Chemical Society*, **2010**. 132(49): 17384-17386.
- [97] Y. Cao, M.S. Denny Jr, J.V. Caspar, W.E. Farneth, Q. Guo, A.S. Ionkin, L.K. Johnson, M. Lu, I. Malajovich, and D. Radu, *Journal of the American Chemical Society*, **2012**. 134(38): 15644-15647.
- [98] S. Kim, J.-S. Park, and A. Walsh, *ACS Energy Letters*, **2018**. 3(2): 496-500.
- [99] Z. Su, K. Sun, Z. Han, H. Cui, F. Liu, Y. Lai, J. Li, X. Hao, Y. Liu, and M.A. Green, *Journal of Materials Chemistry A*, **2014**. 2(2): 500-509.
- [100] J.V. Li, D. Kuciauskas, M.R. Young, and I.L. Repins, *Applied Physics Letters*, **2013**. 102(16): 163905.
- [101] A. Cabas-Vidani, S.G. Haass, C. Andres, R. Caballero, R. Figi, C. Schreiner, J.A. Márquez, C. Hages, T. Unold, and D. Bleiner, *Advanced Energy Materials*, **2018**: 1801191.
- [102] S.G. Haass, C. Andres, R. Figi, C. Schreiner, M. Bürki, Y.E. Romanyuk, and A.N. Tiwari, *Advanced Energy Materials*, **2018**. 8(4): 1701760.
- [103] W. Li, Z. Su, J.M.R. Tan, S.Y. Chiam, H.L. Seng, S. Magdassi, and L.H. Wong, *Chemistry of Materials*, **2017**. 29(10): 4273-4281.
- [104] K.F. Tai, D. Fu, S.Y. Chiam, C.H.A. Huan, S.K. Batabyal, and L.H. Wong, *ChemSusChem*, **2015**. 8(20): 3504-3511.
- [105] Y.-F. Qi, D.-X. Kou, W.-H. Zhou, Z.-J. Zhou, Q.-W. Tian, Y.-N. Meng, X.-S. Liu, Z.-L. Du, and S.-X. Wu, *Energy & Environmental Science*, **2017**. 10(11): 2401-2410.
- [106] Y. Qi, Q. Tian, Y. Meng, D. Kou, Z. Zhou, W. Zhou, and S. Wu, *ACS applied materials & interfaces*, **2017**. 9(25): 21243-21250.
- [107] Z. Su, J.M.R. Tan, X. Li, X. Zeng, S.K. Batabyal, and L.H. Wong, *Advanced Energy Materials*, **2015**. 5(19): 1500682.
- [108] J. Fu, Q. Tian, Z. Zhou, D. Kou, Y. Meng, W. Zhou, and S. Wu, *Chemistry of Materials*, **2016**. 28(16): 5821-5828.

- [109] S. Bag, O. Gunawan, T. Gokmen, Y. Zhu, and D.B. Mitzi, *Chemistry of Materials*, **2012**. 24(23): 4588-4593.
- [110] C.J. Hages, S. Levencenko, C.K. Miskin, J.H. Alsmeier, D. Abou-Ras, R.G. Wilks, M. Bär, T. Unold, and R. Agrawal, *Progress in Photovoltaics: Research and Applications*, **2015**. 23(3): 376-384.
- [111] T. Zhu, W.P. Huhn, G.C. Wessler, D. Shin, B. Saparov, D.B. Mitzi, and V. Blum, *Chemistry of Materials*, **2017**. 29(18): 7868-7879.
- [112] C. Wang, S. Chen, J.-H. Yang, L. Lang, H.-J. Xiang, X.-G. Gong, A. Walsh, and S.-H. Wei, *Chemistry of Materials*, **2014**. 26(11): 3411-3417.
- [113] E. Chagarov, K. Sardashti, A.C. Kummel, Y.S. Lee, R. Haight, and T.S. Gershon, *The Journal of Chemical Physics*, **2016**. 144(10): 104704.
- [114] T. Gershon, K. Sardashti, O. Gunawan, R. Mankad, S. Singh, Y.S. Lee, J.A. Ott, A. Kummel, and R. Haight, *Advanced Energy Materials*, **2016**. 6(22): 1601182.
- [115] W. Zhao, G. Wang, Q. Tian, L. Huang, S. Gao, and D. Pan, *Solar Energy Materials and Solar Cells*, **2015**. 133: 15-20.
- [116] D. Shin, T. Zhu, X. Huang, O. Gunawan, V. Blum, and D.B. Mitzi, *Advanced Materials*, **2017**. 29(24): 1606945.
- [117] D. Shin, B. Saparov, T. Zhu, W.P. Huhn, V. Blum, and D.B. Mitzi, *Chemistry of Materials*, **2016**. 28(13): 4771-4780.
- [118] J. Ge, P. Koirala, C.R. Grice, P.J. Roland, Y. Yu, X. Tan, R.J. Ellingson, R.W. Collins, and Y. Yan, *Advanced Energy Materials*, **2017**. 7(6): 1601803.
- [119] D.B. Khadka and J. Kim, *The Journal of Physical Chemistry C*, **2015**. 119(4): 1706-1713.
- [120] S. Sahayaraj, G. Brammertz, B. Vermang, T. Schnabel, E. Ahlswede, Z. Huang, S. Ranjbar, M. Meuris, J. Vleugels, and J. Poortmans, *Solar Energy Materials and Solar Cells*, **2017**. 171: 136-141.
- [121] J. Park, J. Huang, J. Yun, F. Liu, Z. Ouyang, H. Sun, C. Yan, K. Sun, K. Kim, and J. Seidel, *Advanced Energy Materials*, **2018**: 1701940.
- [122] W. Wu, Y. Cao, J.V. Caspar, Q. Guo, L.K. Johnson, R.S. Mclean, I. Malajovich, and K.R. Choudhury, *Applied Physics Letters*, **2014**. 105(4): 042108.
- [123] H. Sun, K. Sun, J. Huang, C. Yan, F. Liu, J. Park, A. Pu, J.A. Stride, M.A. Green,

- and X. Hao, *ACS Applied Energy Materials*, **2017**. 1(1): 154-160.
- [124] X. Cui, K. Sun, J. Huang, C.-Y. Lee, C. Yan, H. Sun, Y. Zhang, F. Liu, M.A. Hossain, and Y. Zakaria, *Chemistry of Materials*, **2018**.
- [125] M. Sousa, A. Da Cunha, J. Teixeira, J. Leitão, G. Otero-Irurueta, and M. Singh, *Solar Energy Materials and Solar Cells*, **2017**. 170: 287-294.
- [126] S. Gao, Y. Zhang, J. Ao, X. Li, S. Qiao, Y. Wang, S. Lin, Z. Zhang, D. Wang, and Z. Zhou, *Solar Energy Materials and Solar Cells*, **2018**. 182: 228-236.
- [127] X. Lin, J. Kavalakkatt, M.C. Lux-Steiner, and A. Ennaoui, *Advanced Science*, **2015**. 2(6): 1500028.
- [128] S. Djokić, *《Electrodeposition and Surface Finishing》*, **2014**, Springer.
- [129] D. Colombara, A. Crossay, L. Vauche, S. Jaime, M. Arasimowicz, P.P. Grand, and P. Dale, *physica status solidi (a)*, **2015**. 212(1): 88-102.
- [130] F. Jiang, S. Ikeda, T. Harada, and M. Matsumura, *Advanced Energy Materials*, **2014**. 4(7): 4.
- [131] S. Ahmed, K.B. Reuter, O. Gunawan, L. Guo, L.T. Romankiw, and H. Deligianni, *Advanced Energy Materials*, **2012**. 2(2): 253-259.
- [132] J. Tao, J. Liu, L. Chen, H. Cao, X. Meng, Y. Zhang, C. Zhang, L. Sun, P. Yang, and J. Chu, *Green Chemistry*, **2016**. 18(2): 550-557.
- [133] J. Ge, J. Jiang, P. Yang, C. Peng, Z. Huang, S. Zuo, L. Yang, and J. Chu, *Solar Energy Materials and Solar Cells*, **2014**. 125: 20-26.
- [134] S. Pawar, B. Pawar, A. Moholkar, D. Choi, J. Yun, J. Moon, S. Kolekar, and J. Kim, *Electrochimica Acta*, **2010**. 55(12): 4057-4061.
- [135] K. Gurav, S. Shin, U. Patil, M. Suryawanshi, S. Pawar, M. Gang, S. Vanalakar, J. Yun, and J. Kim, *Journal of Alloys and Compounds*, **2015**. 631: 178-182.
- [136] M.P. Suryawanshi, U.V. Ghorpade, U.P. Suryawanshi, M. He, J. Kim, M.G. Gang, P.S. Patil, A.V. Moholkar, J.H. Yun, and J.H. Kim, *ACS Omega*, **2017**. 2(12): 9211-9220.
- [137] Q. Han, Y.-T. Hsieh, L. Meng, J.-L. Wu, P. Sun, E.-P. Yao, S.-Y. Chang, S.-H. Bae, T. Kato, and V. Bermudez, *Science*, **2018**. 361(6405): 904-908.
- [138] I. Olekseyuk, I. Dudchak, and L. Piskach, *Journal of alloys and compounds*, **2004**. 368(1-2): 135-143.

- [139] I. Dudchak and L. Piskach, *Journal of alloys and compounds*, **2003**. 351(1-2): 145-150.
- [140] U. Rau and H.-W. Schock, *Applied Physics A*, **1999**. 69(2): 131-147.
- [141] V. Nadenau, U. Rau, A. Jasenek, and H. Schock, *Journal of Applied Physics*, **2000**. 87(1): 584-593.
- [142] M. Turcu, O. Pakma, and U. Rau, *Applied Physics Letters*, **2002**. 80(14): 2598-2600.
- [143] U. Rau, A. Jasenek, H. Schock, F. Engelhardt, and T. Meyer, *Thin Solid Films*, **2000**. 361: 298-302.
- [144] R. Scheer and H.-W. Schock, 《*Chalcogenide photovoltaics: physics, technologies, and thin film devices*》, **2011**, John Wiley & Sons.

국 문 초 록

# 정전류 동시전기증착법으로 제작한 $\text{Cu}_2\text{ZnSn}(\text{S},\text{Se})_4$ 태양전지의 형상 조절 기술

천기범

재료공학부

서울대학교 대학원

본 연구에서는 CZTSSe 태양전지의 동시전기증착 공정에서, 추가적인 후속공정 없이 핵생성 과정을 제어하고 비정상 입자성장을 억제하였다. 또한, 비정상적 입자성장이 주석 함량이 높은 합금의 성긴 핵생성으로부터 비롯된다는 것을 인지하였으며, 강한 전류를 흘려주어 치밀한 고주석 합금의 핵생성을 일으킴으로써 상대적으로 균일하고 평평한 박막을 얻었다. 전기증착된 상태의 박막의 경우 제곱평균제곱근(RMS) 거칠기( $R_{\text{rms}}$ )가  $0.121 \mu\text{m}$  에서  $0.068 \mu\text{m}$  로 감소하였고, 칼코젠화 된 CZTSSe 박막의 경우  $0.197 \mu\text{m}$  에서  $0.140 \mu\text{m}$  로 감소하였다. 거칠기가 제어된 박막으로 만들어진 셀은 향상된  $V_{\text{oc}}$  와 fill factor를 보였으며, 이

는 계면에서의 재결합이 억제되었기 때문으로 보인다. 순간광전압감쇄법과 온도에 따른  $V_{oc}$  측정 데이터는 계면 재결합이 감소되었음을 시사하였다. 최고 소자 효율은 8.63%였다. 이러한 방법은 전기증착 기반 CZTSSe 태양전지의 계면재결합을 기하학적 측면에서 감소시키는데 효과적이며, 거칠기 제어 관점에서 다중접합 태양전지의 하부 셀에 적용될 수 있는 기술이다.

**주요어:** CZTSSe, 동시전기증착, 핵생성, 거칠기, 계면 재결합

**학 번:** 2017-23429